Monthly Notices of the ROYAL ASTRONOMICAL SOCIETY

MNRAS **500,** 4685–4702 (2021) doi:10.1093/mnras/staa3538
Advance Access publication 2020 November 13

The evolution of the low-frequency radio AGN population to $z \simeq 1.5$ in the ELAIS N1 field

E. F. Ocran [1,2,3★] A. R. Taylor,[1,2,3★] M. Vaccari [2,3,4★] C. H. Ishwara-Chandra,[3,5★] I. Prandoni [4] M. Prescott [2,3] and C. Mancuso[4]

[1]*Department of Astronomy, University of Cape Town, Private Bag X3, Rondebosch 7701, South Africa*
[2]*Department of Physics and Astronomy, University of the Western Cape, Private Bag X17, Bellville 7535, South Africa*
[3]*Inter-University Institute for Data Intensive Astronomy, Private Bag X3, Rondebosch 7701, South Africa*
[4]*INAF – Istituto di Radioastronomia, via Gobetti 101, I-40129 Bologna, Italy*
[5]*National Centre for Radio Astrophysics, Tata Institute of Fundamental Research, Pune 411007, India*

Accepted 2020 November 10. Received 2020 November 10; in original form 2020 March 6

ABSTRACT

We study the cosmic evolution of radio sources out to $z \simeq 1.5$ using a GMRT 610 MHz survey covering $\sim$1.86 deg^2 of the ELAIS N1 field with a minimum/median rms noise 7.1/19.5 μJy beam^{-1} and an angular resolution of 6 arcsec. We classify sources as star forming galaxies (SFGs), radio-quiet (RQ) and radio-loud (RL) Active Galactic Nuclei (AGNs) using a combination of multiwavelength diagnostics and find evidence in support of the radio emission in SFGs and RQ AGN arising from star formation, rather than AGN-related processes. At high luminosities, however, both SFGs and RQ AGN display a radio excess when comparing radio and infrared star formation rates. The vast majority of our sample lie along the SFR $- M_\star$ 'main sequence' at all redshifts when using infrared star formation rates. We derive the 610 MHz radio luminosity function for the total AGN population, constraining its evolution via continuous models of pure density and pure luminosity evolution with $\Phi^\star \propto (1+z)^{(2.25\pm0.38)-(0.63\pm0.35)z}$ and $L_{610\,\mathrm{MHz}} \propto (1+z)^{(3.45\pm0.53)-(0.55\pm0.29)z}$, respectively. For our RQ and RL AGN, we find a fairly mild evolution with redshift best fitted by pure luminosity evolution with $L_{610\,\mathrm{MHz}} \propto (1+z)^{(2.81\pm0.43)-(0.57\pm0.30)z}$ for RQ AGN and $L_{610\,\mathrm{MHz}} \propto (1+z)^{(3.58\pm0.54)-(0.56\pm0.29)z}$ for RL AGN. The 610 MHz radio AGN population thus comprises two differently evolving populations whose radio emission is mostly SF-driven or AGN-driven, respectively.

Key words: galaxies: active – galaxies: luminosity function – large-scale structure of Universe – radio continuum: galaxies.

1 INTRODUCTION

From an observational point of view, active galactic nuclei (AGNs) can be defined as apparent stellar sources with non-thermal spectra and high bolometric luminosity ($\gtrsim 10^{42}$ergs^{-1}) that can exceed that of the host galaxy (e.g. see Bower et al. 2006; Croton et al. 2006; Bonzini et al. 2013; Padovani 2016). An AGN emits radiation at all wavelengths, from radio to X/γ-rays. The non-stellar nature of the radiation emitted by an AGN is understood to result from the accretion of matter on to a supermassive black hole at the centre of its host galaxy, with AGN properties depending on their evolutionary stage and on the rate of fuelling on to their central engine. The current unified theories of AGNs postulate that there are two physically distinct classes of AGN: radio-loud (RL) and radio-quiet (RQ) AGN (see Wilson & Colbert 1995 and references therein). RL AGN produce large-scale radio jets and lobes, with the kinetic power of the jets being a significant fraction of the total bolometric luminosity whereas the weak radio ejecta of the RQ AGN are energetically insignificant (e.g. see Neugebauer et al. 1986; Rawlings & Saunders 1991; Steidel & Sargent 1991). Observationally, RQ AGN are thus radio sources that primarily show signs of AGN activity at other bands (IR, optical, or X-ray) and only a minority of them show the classical large-scale radio structures (jets and lobes) associated with RL AGN (Padovani 1993; Padovani et al. 1993). A multitude of studies have compared the properties of these two AGN classes in various bands to try and shed light on their inherent differences.

To investigate the circumstances under which these two AGN classes originate, it is important to disentangle the radio emission mechanisms involved which will help in the understanding of the connection between AGN and star formation activity. It has been proposed that RQ AGN represent scaled-down versions of RL AGN with mini radio jets (Giroletti & Panessa 2009; Bonzini et al. 2013; Delvecchio et al. 2017). Other studies have argued that the radio emission of RQ AGN come from star formation in the host galaxy (Kimball et al. 2011; Padovani et al. 2011). Dunlop et al. (2003) found that the host galaxies of these two AGN classes are also different, with those of RL AGN mostly hosted by passive ellipticals while those of RQ AGN, excluding the most powerful ones, being spirals. Bonzini et al. (2013) showed that RQ AGN can have host galaxy properties very similar to SFGs, especially where the AGN emission is obscured by dust in the so-called 'type II' objects. Bonzini et al. (2013) used a simple scheme to disentangle SFGs, RQ, and RL AGN based on the combination of radio data with *Chandra* X-ray data and mid-infrared observations from *Spitzer*. Although the RL/RQ AGN classification problem is complex, it appears nevertheless to be solvable. Padovani

★ E-mail: ocran62@gmail.com (EFO); russ@idia.ac.za (ART); mattia.vaccari@gmail.com (MV); ishwar@ncra.tifr.res.in (CHI-C)

(2016) suggested that to classify faint radio sources, one first selects RL AGN using a variant of the infrared-radio correlation and then separates the RQ AGN from SFGs using X-ray luminosity. The far-infrared-colour diagram is then used to recover (RQ) AGN missed by the X-ray criterion. However, Padovani (2016) made mention of the fact that it is important to consider the various, sometimes subtle, selection effects that can plague these studies. Recent work by Padovani (2017) argued that the relative (and absolute) strength of radio emission in the two classes is just a consequence of the presence (or lack) of strong relativistic jets and called for new and better names such as 'jetted' and 'non-jetted' AGN for RL and RQ AGN, respectively.

Measurement of the evolution of AGN underpins our understanding of galaxy evolution over cosmic time. In this context, radio continuum observations provide key information, mainly through the mechanical feedback produced by radio jets in AGN. Studying the properties of radio AGN over cosmic time and comparing the properties of the two RQ and RL subclasses requires their identification and classification in deep ($\lesssim$1 m Jy) and wide (>1 deg^2) radio surveys, which has been possible only recently (Padovani et al. 2009, 2011; Simpson et al. 2012; White et al. 2015, and references therein). Brown, Webster & Boyle (2001) found strong evolution in the low-luminosity radio population at 1.4 GHz out to $z = 0.55$, and by assuming pure luminosity evolution of the form $L \propto (1+z)^K$ found $3 < K < 5$ for AGN with $10^{23} < L_{1.4}\,\mathrm{GHz} < 10^{25}\,\mathrm{W\,Hz^{-1}}$. Sadler et al. (2007) found significant evolution for AGN with $10^{24} < L_{1.4}\,\mathrm{GHz} < 10^{25}\,\mathrm{W\,Hz^{-1}}$ consistent with pure luminosity evolution where $L \propto (1+z)^{2.0\pm0.3}$ from $z = 0.7$, using the 2SLAQ Cannon et al. (2006) luminous red galaxy survey catalogue combined with Faint Images of the Radio Sky at Twenty-Centimeters (FIRST; Becker, White & Helfand 1995) and NRAO VLA Sky Survey (NVSS; Condon et al. 1998).

Prescott et al. (2016) determined radio luminosity functions at 325 MHz for a sample of radio-loud AGN by matching a 138 deg^2 radio survey conducted with the Giant Metrewave Radio Telescope (GMRT), with optical imaging and redshifts from the Galaxy And Mass Assembly survey (GAMA). By fitting the AGN radio luminosity function out to $z = 0.5$ as a double power law, and parametrizing the evolution as $\Phi \propto (1+z)^K$, they found evolution parameters of $K = 0.92 \pm 0.95$ assuming pure density evolution and $K = 2.13 \pm 1.96$ assuming pure luminosity evolution.

Yuan et al. (2016) proposed a mixture evolution scenario to model the evolution of the radio luminosity function (RLF) of steep spectrum AGN based on a Bayesian method. In this scenario, the shape of the RLF is determined by both the density and luminosity evolution. Based on a sample of over 1800 radio AGN at redshifts out to $z \sim 5$ from 3 GHz radio data in the COSMOS field from the JVLA-COSMOS project, which have typical stellar masses within $\sim 3 \times (10^{10} - 10^{11})\,\mathrm{M_\odot}$, Smolčić et al. (2017) derived the 1.4 GHz radio luminosity functions for radio AGN, out to $z \sim 5$. They defined their radio AGN as all the sources that show a significant radio excess with respect to what is expected from pure SF, independently from the properties of the host galaxies. They constrained the evolution of this population via continuous models of pure density and pure luminosity evolution and found best-fitting parametrizations of $\Phi^\star \propto (1+z)^{(2.00\pm0.18)-(0.60\pm0.14)z}$ and $L^\star \propto (1+z)^{(2.88\pm0.82)-(0.84\pm0.34)z}$, respectively. Ceraj et al. (2018) studied a sample of 1604 moderate-to-high radiative luminosity active galactic nuclei (HLAGNs) selected at 3 GHz by the JVLA-COSMOS project. By assuming pure density and pure luminosity evolution models they constrained their cosmic evolution out to $z \sim 6$, finding $\Phi^\star \propto (1+z)^{(2.64\pm0.10)-(0.61\pm0.04)z}$ and $L^\star \propto (1+z)^{(3.97\pm0.15)-(0.92\pm0.06)z}$. These several studies, while clearly showing evolution, yield different quantitative results and identify the AGN population with differing selection strategies and redshift range. Here we explore the evolution of AGN based on the faint low-frequency radio population out to $z \simeq 1.5$, distinguish RQ and RL AGN and compare to the evolution of SFG from the same radio sample.

This is the third paper exploiting our deep 610 MHz GMRT observations of the ELAIS N1 field, covering $\sim$1.86 deg^2 down to a minimum rms noise of $\sim$7.1 μJy beam^{-1}. Our previous work demonstrated the importance of using deep radio surveys as a tool to study the cosmic star formation history. In this work, we extend our analysis to the AGN population. Our AGN population includes RQ AGN and RL AGN classified using multiwavelength data. We study the infrared-radio correlation for the RQ AGN and RL AGN populations in comparison to the SFG population, the evolution low-frequency radio emission to $z \sim 1.5$, and we investigate the relation between star formation rates (SFR) and stellar masses of the host galaxies. The layout of the paper is as follows: we first introduce the 610 MHz GMRT data and our AGN sample in Section 2. In Section 3, we present the analysis and the results obtained from our AGN sample, comparing them to the SFGs we presented in Ocran et al. (2020a,b). The sample selection for estimation of the AGN luminosity function and the method applied is discussed in Section 4. Also, we describe how we constrain the evolution of the AGN luminosity function out to $z \simeq 1.5$. We discuss the evolution of our AGN sample in Section 5. We summarize our results and discuss future work in Section 6. We adopt throughout the paper a flat concordance Lambda cold dark matter (ΛCDM) cosmology with the following parameters: Hubble constant $H_0 = 70\,\mathrm{kms^{-1}\,Mpc^{-1}}$, dark energy density $\Omega_\Lambda = 0.7$, and matter density $\Omega_\mathrm{m} = 0.3$.

2 SAMPLE

2.1 GMRT 610 MHz data

For our analysis, we employ our 610 MHz radio survey covering 1.86 deg^2 of the ELAIS N1 field carried out with the GMRT. This is currently the deepest low-frequency radio survey at 610 MHz. We achieve a minimum noise of 7.1 μJy beam^{-1} and an angular resolution of 6×6 arcsec^2, with the median noise over the 1.86 deg^2 being 19.5 μJy beam^{-1}. The higher median noise value results primarily from the lower sensitivity around the edges of the mosaic image (see Ocran et al. 2020a). The radio imaging, reduction, source extraction, multiwavelength association, and classification process is described in detail in Ocran et al. (2020a). A shallower image covering a much larger area of 12.8 deg^2 of the ELAIS N1 field at 610 MHz to an rms noise of $\sim$40 μJy beam^{-1} was recently obtained by Ishwara-Chandra et al. (2020)

2.2 AGN sample

Our AGN sample is defined as the sample of 610 MHz sources with at least one AGN indicator. As described in Ocran et al. (2020a,b) we used radio and X-ray luminosity, optical spectroscopy, mid-infrared colours, and IR to radio flux ratios to separate the radio source population with a multiwavelength association and a redshift estimate into three classes: SFGs, RQ AGN, and RL AGN (see also Ocran et al. 2017). If an AGN is not present in the source according to any of the several criteria, then we inferred that the source was an SFG. We thus have employed a combination of multiwavelength AGN diagnostics to obtain a census of galaxies showing evidence of

Table 1. Total number of SFGs, RQ AGN, and RL AGN.

SFGs	RL AGN	RQ AGN
1685	339	281

hosting an AGN. Our sample of AGN includes sources with reliable redshift that have been classified as AGN in at least one of the multiwavelength diagnostics.

Once AGN are classified, the distinction between RQ and RL AGN is based on q_{24}, the logarithmic flux density ratio between the infrared (i.e. MIPS 24 micron flux) and radio, quantified by Appleton et al. (2004) as

$$q_{24} = \log_{10}\left(\frac{S_{24}}{S_{\rm radio}}\right). \quad (1)$$

To classify the sources, we follow Bonzini et al. (2013) who used the q_{24} versus redshift to separate their various populations by defining a locus for SFG and computing q_{24} as a function of z using the SED of M82 (Polletta et al. 2007) as representative of their SFGs. They normalized the M82 template to the local average value of q_{24} as obtained in Sargent et al. (2010) (see Bonzini et al. 2013 for more details) and classified objects with radio excess as RL AGN below the SFG locus. Objects within the SFG locus were classified as RQ AGN if it shows clear evidence for an AGN in the X-ray or in the MIR bands otherwise, they adopted an SFG classification. We used the normalized M82 template in the q_{24}, z plane, the dividing line between RQ and RL AGN. We classified objects as RL AGN as all sources with q_{24} below the SFG locus. Above this threshold, we classify a source as an RQ AGN if it shows clear evidence for an AGN in X-ray luminosity, optical spectroscopy, from its radio power, or from its IRAC colours satisfying the Donley et al. (2012) criterion. When the above conditions were not met, an SFG classification is adopted.

As detailed in Ocran et al. (2020a,b), the total number of sources with redshifts for which we can define at least one AGN indicator is 2305. This constitutes 74 per cent of the 3105 sources with secure redshifts and 54 per cent of the total 4290 sources presented in Ocran et al. (2020a) covering $\sim$1.86 deg^2 of the ELAIS N1 field. Redshift estimates used in this work are a combination of spectroscopic and photometric redshifts from the Hyper Suprime-Cam (HSC) Photometric Redshift Catalogue (Tanaka et al. 2018), the revised SWIRE Photometric Redshift Catalogue (Rowan-Robinson et al. 2013), and the Herschel Extragalactic Legacy Project (HELP; Vaccari 2016; Shirley et al. 2019). Table 1 presents the total number of SFGs, RQ AGN, and RL AGN from our classification scheme. From 2305 sources at 610 MHz in ELAIS N1 with secure redshifts, 1685 (73 per cent) are SFGs, while 620 (27 per cent) are AGN. Within our AGN sample 281 (45 per cent) sources were classified as RQ AGN whereas 339 (55 per cent) were classified as RL AGN.

Fig. 1 shows the distribution of the SFGs (grey histogram), total AGN (green histogram), RL AGN (red histogram), and RQ AGN (blue histogram) with 610 MHz luminosity (left-hand panel), redshift (middle panel), and $r_{\rm AB}$ (from Tanaka et al. 2018) (right-hand panel). The distribution for SFGs in each panel is scaled down by a factor of five to ease comparison with AGN distributions. The dashed vertical black line shows the magnitude limit of $r = 25$ we apply to our sample in Section 4 for the redshift completeness (see Section 4 for more details).

In Fig. 2 we illustrate how the different classes populate the mid-infrared colour–colour space. The left-hand panel shows the IRAC colour–colour regions first adopted by Lacy et al. (2004). The four regions separated by dashed lines in the diagram are labelled based on the modelling by Sajina et al. (2005). Region 1 selects sources where the infrared emission is dominated by non-equilibrium emission of very small dust grains, which is interpreted as polycyclic aromatic hydrocarbon (PAH) destruction by the hard ultraviolet spectrum of an AGN. Region 2 is mainly populated by dusty star-forming galaxies at redshift $z < 0.5$ with strong PAH bands, as the 3.6 and 8.0 μm flux contain the strongest PAH features at low redshift. Region 3 can be divided into two as denoted by Taylor et al. (2007) and Banfield et al. (2011): (i) where the region is populated by elliptical galaxies dominated by the starlight of old stellar populations (i.e $\log_{10}(S_{8.0}/S_{4.5}) \leq -0.5$); and (ii) where the region is populated by galaxies with fainter PAH emission (i.e $\log_{10}(S_{8.0}/S_{4.5}) > -0.5$) (see left-hand panel of Fig. 2). The grey shaded area represents the more restrictive AGN selection criteria presented by Donley et al. (2012), which is fully included within Region 1 and which we adopted in our work. The vast majority of our RQ AGN falls within Region 1 and primarily within the smaller Donley et al. (2012) region. RL AGN are concentrated in Region 3, albeit with a non-negligible number falling within the lower left of Region 1. The vast majority of SFGs span Region 1 and Region 2.

The right-hand panel of Fig. 2 shows the IRAC colour–colour plot first adopted by Richards et al. (2006), who suggested that type 1 quasars may be selected by taking $[3.6] - [4.5] = -2.5\log(S_{3.6}/S_{4.5}) > -0.1$, indicated by the grey shaded area in the plot. The plot shows that the vast majority of our RQ AGN falls within the region of type 1 quasars, whereas most of our RL AGN fall outside the region. SFGs span both regions, with some of them likely harbouring hidden low-luminosity type 1 AGN.

3 ANALYSIS AND RESULTS

3.1 The infrared-radio correlation (IRRC)

It has long been known that the ratio of infrared and radio luminosity in SFGs follows a tight empirical relation. This so-called IR/radio correlation (IRRC) is well-established using a variety of ways to measure infrared and radio luminosities (see e.g. Dickey & Salpeter 1984; de Jong et al. 1985; Bell et al. 2003). In Ocran et al. (2020b), we studied the IRRC for our SFGs using the IR bolometric (i.e. integrated between 8 and 1000 μm) luminosity and the 1.4 GHz radio luminosity given by equation (2) (see also Ocran et al. 2017).

$$q_{\rm IR} = \log_{10}\left(\frac{L_{\rm IR}}{3.75\times10^{12}\,{\rm W}}\right) - \log_{10}\left(\frac{L_{\rm radio}}{{\rm W\,Hz^{-1}}}\right). \quad (2)$$

In this work, we extend our IRRC analysis to RQ and RL AGN in comparison to SFGs. The SFGs used in this work is based on the subsample presented in Ocran et al. (2020b).

In Fig. 3, we plot rest-frame 610 MHz luminosity versus the IR bolometric luminosity for each source class in comparison to the IRRC. The diagonal solid line in each panel shows the median $q_{\rm IR}$ at 610 MHz for the SFGs, since the IRRC is believed to be driven mostly by star formation (Condon 1992; Yun, Reddy & Condon 2001). The dashed diagonal lines represent the $\pm1\sigma$ limits given by the median absolute deviation (MAD) (Rousseeuw & Croux 1993), $\sigma_{\rm q_{IR\,SF}} = 0.30$, of the correlation. The contours levels are 1σ, 2σ, 3σ, and 4σ. We reported a median $q_{\rm 610\,MHz}$ of 2.32 for our SFGs (see Ocran et al. 2020b). RQ AGN exhibit a moderately tight correlation with the IRRC, with a median $q_{\rm IR}$ value of 2.10 (MAD = 0.34). Excess radio emission is evident at higher luminosities. Our RL AGN lie well above the median value of the IRRC for SFGs because of the additional AGN component to radio emission. We measure a median $q_{\rm IR}$ value for RL AGN to be 1.75 (MAD = 0.40).

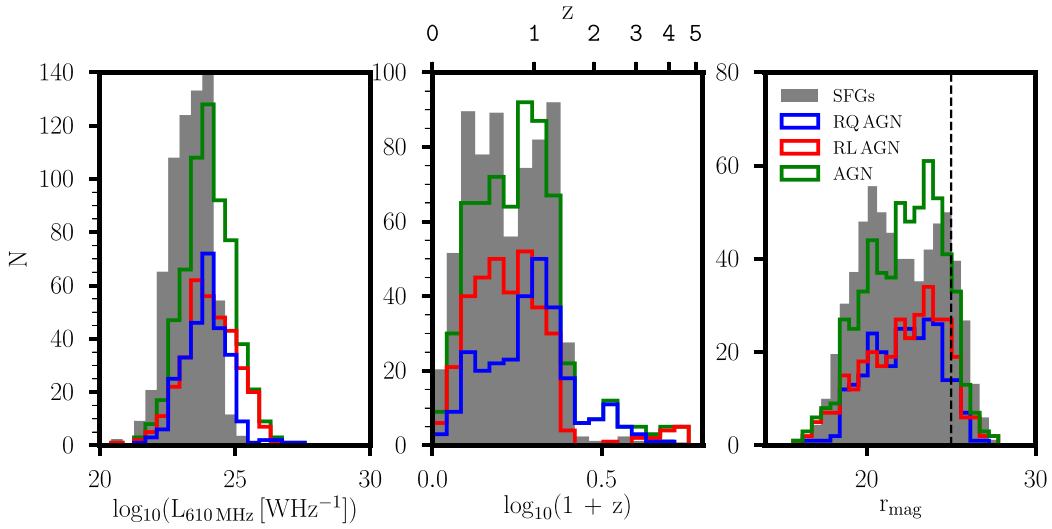

Figure 1. Distribution of the SFGs (grey histogram), total AGN (green histogram), RL AGN (red histogram), and RQ AGN (blue histogram) with 610 MHz luminosity (left-hand panel), redshift (middle panel), and r_{AB} (right-hand panel). The distribution for SFGs in each panel is scaled down by a factor of five to ease comparison with the AGN distributions. The dashed vertical black line in the right-hand panel shows the magnitude limit of $r = 25$, we apply to our sample in Section 4 for redshift completeness.

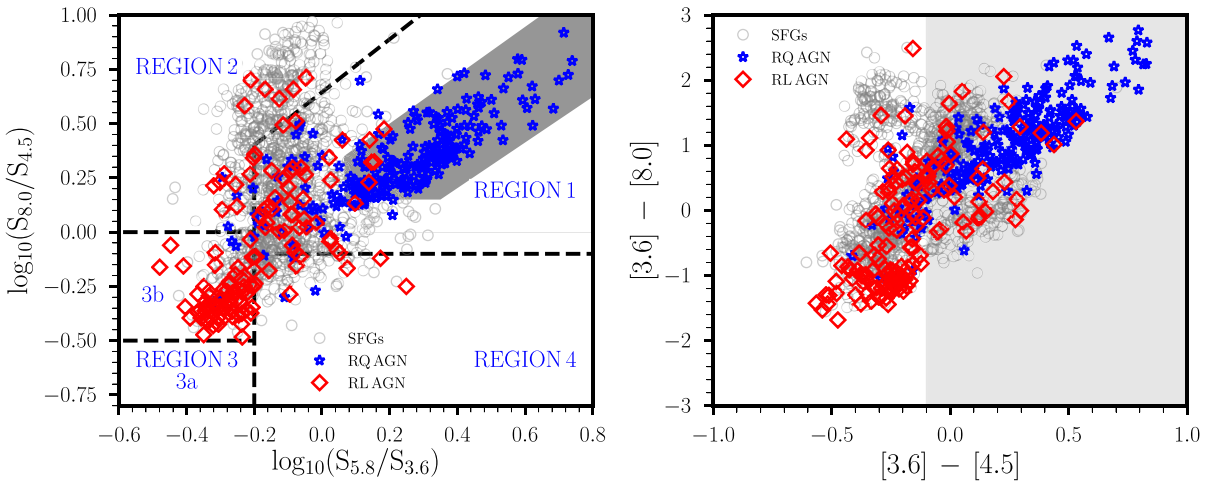

Figure 2. Mid-infrared colours of our radio populations. Left-hand panel: IRAC colour–colour plot by Lacy et al. (2004) for SFGs, RQ AGN, and RL AGN with four-band IRAC detections. The four regions outlined by dashed lines are the ones defined by Sajina, Lacy & Scott (2005) whilst the grey shaded area defines the AGN criterion by Donley et al. (2012). Right-hand panel: IRAC colour–colour plot by Richards et al. (2006) for SFGs, RQ AGN, and RL AGN with four-band IRAC detections. The grey shaded region shows the Richards et al. (2006) type 1 quasars selection.

Table 2 summarizes the median values of q_{IR} at 610 MHz for SFGs, RQ AGN, and RL AGN. Assuming a fixed value of spectral index $\alpha = -0.8$, to convert radio luminosity between 610 and 1400 MHz, gives the simple conversion $q_{610\,MHz} = q_{1.4GHz} - 0.29$ (see subsection 3.1 of Ocran et al. 2020b). With this assumption, the median values of q_{IR} at 1.4 GHz for our SFGs, RQ, and RL AGN samples are 2.61 ± 0.30, 2.39 ± 0.34, and 2.04 ± 0.40, respectively.

3.2 Radio emission in the faint low-frequency radio source population

The origin of the radio emission in RQ AGN is vigorously debated. Bonzini et al. (2015) compared the SFR computed from IR luminosity with the SFR derived from radio luminosity for their 675 radio sources and observed a good agreement between SFR_{radio} and SFR_{IR} for RQ AGN. More recent work by Delvecchio et al. (2017) exploited multiband information in the COSMOS field to derive accurate SFR via SED fitting. They analysed the ratio between the 1.4 GHz radio luminosity and the SFR for each source and found that ∼30 per cent of the sources with AGN signatures at non-radio wavelengths display a significant radio excess. Recent modelling work by Mancuso et al. (2017) supports the likely scenario that RQ AGN are composite systems where SF- and AGN-triggered radio emission can coexist over a wide range of relative contributions.

We characterize the star formation properties of the three types of sources by investigating IR and radio-based SFR, presented in Fig. 4. The IR star formation rates were obtained by the Herschel Extragalactic Legacy Project (HELP; Vaccari 2016; Hurley et al.

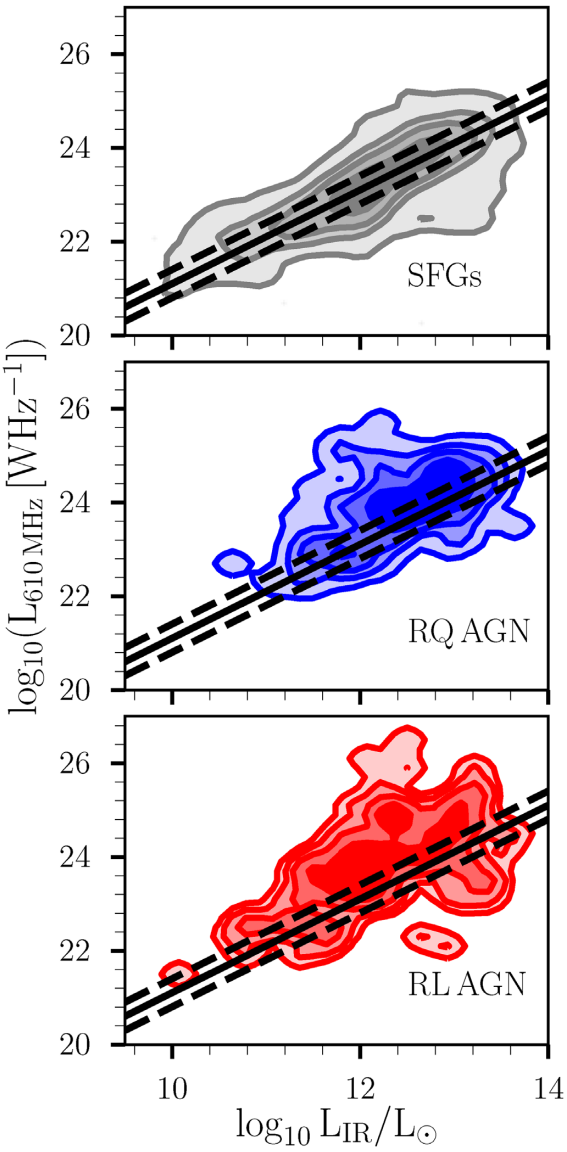

Figure 3. Rest-frame 610 MHz luminosity as a function of IR luminosity for SFGs (top panel), RQ AGN (middle panel), and RL AGN (bottom panel) represented as density contours. These contours represent the density distribution of the sources in the $\log_{10} L_{610\,\mathrm{MHz}}$ versus $\log_{10} L_{\mathrm{IR}}$ plane. The solid line shows the IRRC with a q_{IR} value equal to the mean SF-powered q_{IR} of 2.32 (see Ocran et al. 2020b), with the dashed lines representing the $\pm 1\sigma$ limits, $\sigma_{\mathrm{qSF}} = 0.30$ of the correlation.

Table 2. Table summarizing the median values of q_{IR} at 610 MHz for SFGs, RQ AGN, and RL AGN.

Median $q_{\mathrm{IR\,SFG}}$	Median $q_{\mathrm{IR\,RQ\,AGN}}$	Median $q_{\mathrm{IR\,RL\,AGN}}$
2.32 ± 0.30	2.10 ± 0.34	1.75 ± 0.40

2017; Małek et al. 2018; Shirley et al. 2019), which collected multiwavelength photometry and performed homogeneous physical modelling over roughly 1300 deg^2 of extragalactic sky covered by the Herschel Space Observatory's SPIRE Camera (Griffin et al. 2010; Pilbratt et al. 2010), focusing on ELAIS N1 as a pilot field. Małek et al. (2018) computed the stellar masses, SFRs, and dust properties from the large multiwavelength catalogues of galaxies by fitting

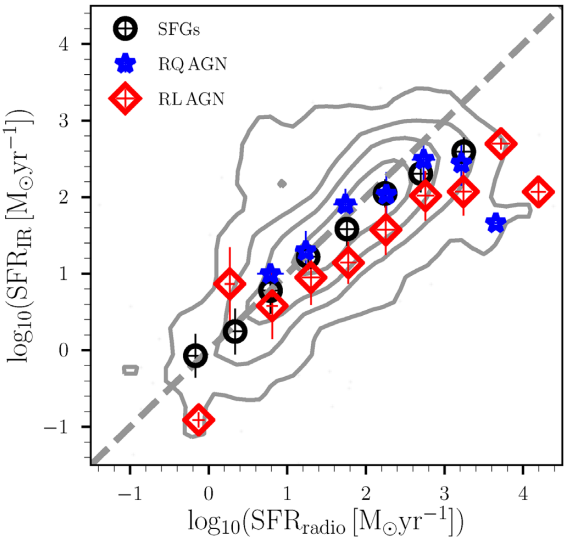

Figure 4. Binned $\log_{10}(\mathrm{SFR_{IR}})$ versus $\log_{10}(\mathrm{SFR_{radio}})$ for the SFGs, RQ AGN, and RL AGN in bin width of $0.5\log_{10}(\mathrm{SFR_{IR}})$. The background contours represents the density distribution of sources in the $\log_{10}(\mathrm{SFR_{IR}})$ versus $\log_{10}(\mathrm{SFR_{radio}})$ plane for our subsample (i.e both the SFGs and AGN) with SFR estimates. The dashed grey line corresponds to $\log_{10}(\mathrm{SFR_{IR}}) = \log_{10}(\mathrm{SFR_{radio}})$.

physical models to the galaxy's broad-band SED. They used the Code Investigating GAlaxy Emission (Boquien et al. 2019) to estimate these physical parameters by comparing modelled galaxy SEDs to observed ones. The $\mathrm{SFR_{radio}}$ given by equation (3) below,

$$\left(\frac{\mathrm{SFR_{radio})}}{\mathrm{M_{\odot}\,yr^{-1}}}\right) = \mathcal{F}_{\mathrm{IMF}} \times 10^{-24}\, 10^{q_{\mathrm{IR}}(z)} \left(\frac{L_{610\,\mathrm{MHz}}}{\mathrm{WHz^{-1}}}\right) \quad (3)$$

was computed using the redshift-dependent $q_{\mathrm{IR}}(z)$ parameter accounting for intrinsic observational limitations under the assumption of a linear IR-radio correlation (see section 6 of Ocran et al. 2020b). We used the Chabrier (2003) IMF.

Fig. 4 shows the binned $\log_{10}(\mathrm{SFR_{IR}})$ versus $\log_{10}(\mathrm{SFR_{radio}})$ for SFGs, RQ AGN, and RL AGN in bin width of $0.5\log_{10}(\mathrm{SFR_{IR}})$. It should be noted that $\mathrm{SFR_{radio}}$ is obtained under the assumption that the radio emission is entirely ascribed to star formation. The radio and IR rest-frame correlates rather well across a wide range of luminosities for both SFGs and RQ AGN as shown in Fig. 4. While for the RL AGN there is a radio excess, as expected from the classification presented in Section 2.2. This strongly suggests that the two quantities are equivalently good tracers of the SFR and that the main contribution to the radio emission in RQ AGN is due to the star-formation in the host galaxy rather than being powered by black hole activity. The behaviour of the RL AGN further supports this hypothesis since they scatter out from the one-to-one relation in Fig. 4. This can be attributed to the fact that for RL AGN the SFRs computed from the radio luminosity is overestimated due to the jet contribution to the radio emission. Note that the comparison of the two SFR tracers can in principle also allow us to isolate sources that have been misclassified.

At the high end of the radio-based SFR estimate (i.e. for $\log_{10}\mathrm{SFR_{radio}} > 2.8$) there are indications of a radio excess in the SFR of all population, as the SFR tracers for all the populations tend to deviate from the one-to-one line. A plausible interpretation of this behaviour is the possibility of contamination of the RQ AGN population from RL AGN with a contribution to the 24 μm flux

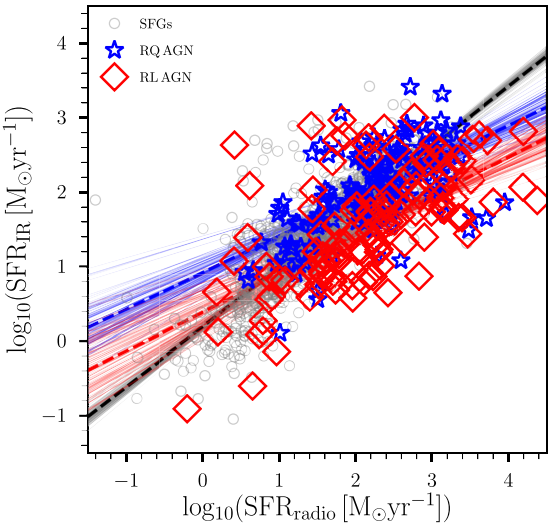

Figure 5. SFR derived from the IR luminosity versus the SFR from the radio luminosity. SFGs are plotted as open grey circles, RQ AGN as open blue stars, and RL AGN as open red diamonds. A linear regression line that we get from each bootstrap replicate of the slope and intercept to each population are represented as light blue for RQ AGN, light red for RL AGN, and grey for SFGs. The median of each bootstrap are represented as solid dashed lines.

density that enhanced their value into the SFGs locus, since our distinction between RL and RQ AGN is based on q_{24} (see Ocran et al. 2017, 2020a). We also note that the deviation from the IRRC (see subsection 3.1) seems to become larger going to higher luminosities. This may offer another interpretation, i.e. that only QSO-like objects host mini-jets while in lower luminosity sources radio emission is originated by star formation. This might be in line with recent results from White et al. (2017) on optically selected QSOs, where they found a radio luminosity excess with respect to SFGs that appears to be correlated with the optical luminosity. We see a similar trend in the RL AGN. Our selected SFGs have typical $\mathrm{SFR_{IR}}$ of 1.46 $\mathrm{M_\odot\ yr^{-1}}$ with an MAD of 0.49 $\mathrm{M_\odot\ yr^{-1}}$ and $\mathrm{SFR_{radio}}$ of 1.71 $\mathrm{M_\odot\ yr^{-1}}$ with an MAD of 0.54 $\mathrm{M_\odot\ yr^{-1}}$. The RL AGN have on average slightly higher SFRs than SFGs, with a median $\mathrm{SFR_{IR}}$ of 1.57 $\mathrm{M_\odot\ yr^{-1}}$ (MAD = 0.57 $\mathrm{M_\odot\ yr^{-1}}$) and a median $\mathrm{SFR_{radio}}$ of 2.37 $\mathrm{M_\odot\ yr^{-1}}$ (MAD = 0.67 $\mathrm{M_\odot\ yr^{-1}}$). RQ AGN hosts have SFRs higher than SFGs hosts with a median $\mathrm{SFR_{IR}}$ of 2.02 $\mathrm{M_\odot\ yr^{-1}}$ (MAD = 0.39 $\mathrm{M_\odot\ yr^{-1}}$) and a median $\mathrm{SFR_{radio}}$ of 2.27 $\mathrm{M_\odot\ yr^{-1}}$ (MAD = 0.53 $\mathrm{M_\odot\ yr^{-1}}$).

Fig. 5 compares the SFR computed from IR luminosities with the expected SFR as derived from the radio luminosities for our individual SFGs, RQ AGN, and RL AGN for which we have performed bootstrapped linear regression[1] fits to each subpopulation. Different colours and symbols represent different classes of objects. The results of the linear regression fit are

$$\log_{10}(\mathrm{SFR_{IR}})_{\mathrm{SFG}} = 0.81^{+0.03}_{-0.03} \times \log_{10}(\mathrm{SFR_{radio}})_{\mathrm{SFG}} + 0.20^{+0.04}_{-0.05} \quad (4)$$

$$\log_{10}(\mathrm{SFR_{IR}})_{\mathrm{RQ\,AGN}} = 0.50^{+0.07}_{-0.06} \times \log_{10}(\mathrm{SFR_{radio}})_{\mathrm{RQ\,AGN}} + 0.93^{+0.15}_{-0.15} \quad (5)$$

$$\log_{10}(\mathrm{SFR_{IR}})_{\mathrm{RL\,AGN}} = 0.52^{+0.08}_{-0.07} \times \log_{10}(\mathrm{SFR_{radio}})_{\mathrm{RL\,AGN}} + 0.40^{+0.19}_{-0.22}. \quad (6)$$

[1] A resampling method used to estimate the variability of statistical parameters from a data set which is repeatedly sampled with replacement (Lopes, Wang & Mahoney 2019).

The fits for the RL AGN (dashed red line) and RQ AGN (dashed blue line) from Fig. 5 show a similar slope. Both fits are flatter than the SFG fit. This is not a surprise as in both cases deviations from the IRRC are stronger going to higher luminosities. This again supports the idea that there is a fraction of RQ AGN hosting mini radio jets. And this fraction increases with luminosity. Despite similar slopes, RL and RQ AGN fits differ by an offset, which points towards RQ AGN being hosted, on average, by higher SFR galaxies. This is further supported by Fig. 6, which shows the host galaxy IR-derived SFR distribution in four different redshift bins for RL and RQ AGN. AGN host galaxies span a very wide range of SFRs, with RQ AGN generally hosted by higher SFR galaxies and RL AGN (which are mainly at low redshifts) hosted predominantly by galaxies with low SFRs. Also, there is evidence of an IR excess in the RQ AGN population from Fig. 6. Table 3 presents median values of the $\mathrm{SFR_{IR}}$ for the RQ AGN, RL AGN, and SFGs in each redshift bin. The errors denote the difference between the 15.8 and 84.2 percentiles.

3.3 SFR versus stellar mass

The SFR of SFGs is tightly correlated with the stellar mass of the galaxy by the so-called 'main sequence (MS) for star forming galaxies' (Brinchmann et al. 2004; Salim et al. 2007). The correlation reveals interesting mechanisms of the star formation history. A high scatter in this correlation implies a stochastic star formation history with many discrete 'bursts', while a tighter correlation implies a star formation history that traces stellar mass growth more smoothly (see e.g. Daddi et al. 2007; Renzini 2009; Lee et al. 2012). Previous studies have shown that the MS for SFGs has near-constant slope but shifts towards higher SFRs as the redshift increases (see e.g. Elbaz et al. 2007; Noeske et al. 2007; Rodighiero et al. 2011; Johnston et al. 2015). The MS for SFGs is largely linear and has remarkably small scatter at low redshifts (see Brinchmann et al. 2004).

In the left-hand panel of Fig. 7 we show $\mathrm{SFR_{IR}}$, which is relatively immune fron AGN contamination compared to $\mathrm{SFR_{radio}}$, as a function of galaxy stellar mass for our objects divided in four redshift bins on the left-hand panel. In comparison, in the right-hand panel we also present the $\mathrm{SFR_{radio}}$ as a function of galaxy stellar mass for our objects divided in four redshift bins (see right-hand panel of Fig. 7). Table 4 presents the median values of the stellar masses for the RQ AGN, RL AGN, and SFGs in each redshift bin (see the dashed red and blue vertical lines in Fig. 7 that represents the median values in Table 4). The black dashed lines indicate the expected position of the SFMS at the average redshift of the sources in each bin.

We describe the redshift evolution of the SFMS by following the law:

$$\log_{10}(\mathrm{SFR}(M_\star, z)) = 7.77 + 0.79 \times \log_{10}(M_\star) + 2.8 \times \log_{10}(1+z), \quad (7)$$

where SFR is the star formation rate expressed in $M_\odot\ \mathrm{yr^{-1}}$, $M_\star$ is the stellar mass expressed in $M_\odot$, and the slope and the redshift evolution are based on the results of Rodighiero et al. (2011). The dot-dashed lines in each panel above and below the MS for SFGS correspond to ±0.6 dex (see Bonzini et al. 2015). The RQ AGN and SFG populations appear to occupy a similar locus in the $M_\star$ − SFR especially up to the third redshift bin (i.e. $0.5 < z < 0.9$) for the $\mathrm{SFR_{IR}}$ versus stellar mass plot. The RL AGN show a larger scatter from the SFMS. This scatter of the RL AGN is more pronounced in the $\mathrm{SFR_{radio}}$ versus stellar mass plot. In subsection 3.2 we showed that there is a deviation from the one-to-one relation in Fig. 4 at the high luminosity end with that of the RL AGN becoming more

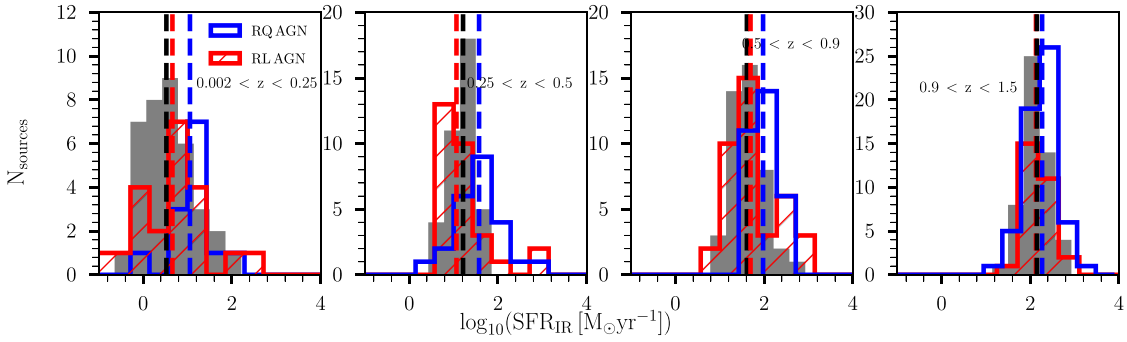

Figure 6. Distribution of infrared-based star formation rates in four redshift bins for RQ AGN (blue histogram) and RL AGN (red histogram). The dashed blue and red vertical lines represents the median values of the SFR_{IR} for the RQ and RL AGN in each redshift bin. The filled grey histograms in each panel represents the SFR distribution for SFGs in each redshift bin scaled by a factor of five to ease the comparison to the RQ and RL distributions. The dashed vertical lines in each panel represents the median values of the SFR_{IR} for the SFGs.

Table 3. Median values of SFR_{IR} for the RQ AGN, RL AGN, and SFGs in each redshift bin. The errors denote the difference between the 15.8 and 84.2 percentiles.

Redshift range	$N_{RQ\,AGN}$	RQ AGN $\log_{10}\,SFR_{IR}(M_\odot yr^{-1})$	$N_{RL\,AGN}$	RL AGN $\log_{10}\,SFR_{IR}(M_\odot yr^{-1})$	N_{SFG}	SFG $\log_{10}\,SFR_{IR}(M_\odot yr^{-1})$
$0.002 < z < 0.25$	13	$1.06^{+0.25}_{-0.14}$	21	$0.66^{+0.52}_{-0.57}$	214	$0.52^{+0.74}_{-0.56}$
$0.25 < z < 0.5$	24	$1.57^{+0.29}_{-0.37}$	30	$1.06^{+0.48}_{-0.29}$	294	$1.21^{+0.28}_{-0.37}$
$0.5 < z < 0.9$	31	$1.98^{+0.40}_{-0.30}$	39	$1.69^{+0.92}_{-0.48}$	240	$1.61^{+0.42}_{-0.32}$
$0.9 < z < 1.5$	58	$2.27^{+0.30}_{-0.37}$	29	$2.13^{+0.33}_{-0.32}$	273	$2.15^{+0.35}_{-0.27}$

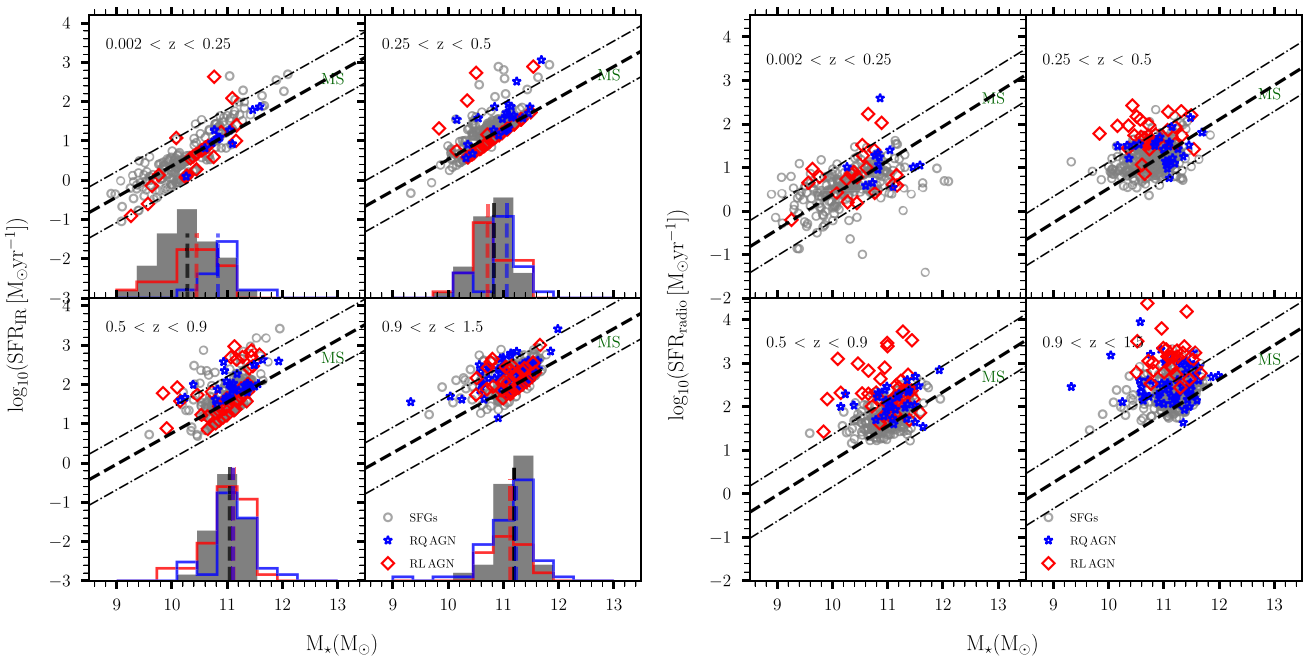

Figure 7. SFR_{IR} versus stellar mass (left-hand panel) and SFR_{radio} versus stellar mass (right-hand panel) for $0.002 < z < 0.25$, $0.25 < z < 0.5$, $0.5 < z < 0.9$, and $0.9 < z < 1.5$ redshift bins. The open grey circles, open red diamonds, and blue stars represent SFGs, RL AGN, and RQ AGN, respectively. The dashed lines indicates the position of the main sequence for SFGs and its redshift evolution as found in Bonzini et al. (2015) at the average redshift of the sources in each bin using equation (7). The dot-dashed lines above and below the SFMS correspond to ±0.6 dex. The grey, red, and blue inset histograms in each panel shows the distribution for the SFGs, RL, and RQ AGN in each redshift bin, respectively. The dashed black, blue, and red vertical lines in each panel represents the median values of the stellar masses for the SFGs, RQ AGN, and RL AGN, respectively.

Table 4. Median values of stellar mass for the RQ AGN, RL AGN, and SFG samples in each redshift bin. The errors denote the difference between the 15.8 and 84.2 percentiles.

Redshift range	$N_{\rm RQ\,AGN}$	RQ AGN $\log_{10} M_\star(\mathrm{M}_\odot)$	$N_{\rm RL\,AGN}$	RL AGN $\log_{10} M_\star(\mathrm{M}_\odot)$	$N_{\rm SFG}$	SFGs $\log_{10} M_\star(\mathrm{M}_\odot)$
$0.002 < z < 0.25$	13	$10.83^{+0.29}_{-0.12}$	21	$10.45^{+0.42}_{-0.61}$	214	$10.28^{+0.58}_{-0.54}$
$0.25 < z < 0.5$	24	$11.06^{+0.21}_{-0.55}$	30	$10.71^{+0.48}_{-0.31}$	294	$10.83^{+0.28}_{-0.38}$
$0.5 < z < 0.9$	31	$11.11^{+0.38}_{-0.28}$	39	$11.11^{+0.25}_{-0.46}$	240	$11.05^{+0.23}_{-0.32}$
$0.9 < z < 1.5$	58	$11.23^{+0.25}_{-0.51}$	29	$11.13^{+0.27}_{-0.34}$	273	$11.20^{+0.26}_{-0.27}$

prominent. For RL AGN the radio SFR exceed the IR SFR for high radio luminosities. This is attributed to the excess radio emission from the AGN. The departure of RL AGN from the locus populated by RQ AGN and SFGs in the $\mathrm{SFR_{radio}}$ versus stellar mass plot (right-hand panel) of Fig. 7 can be attributed to this effect.

To compare the SSFR properties of our three populations in a quantitative manner, we also carried out a two-sample K–S test statistics of the $\mathrm{SFR_{IR}}[\mathrm{M}_\odot\mathrm{yr}^{-1}]/M_\star(\mathrm{M}_\odot)$ and $\mathrm{SFR_{radio}}[\mathrm{M}_\odot\mathrm{yr}^{-1}]/M_\star(\mathrm{M}_\odot)$ distribution of the three source classes in four redshift bins. The results are included in Tables 5 and 6. While the SSFR distribution of SFGs and RL AGNs is conclusively shown to be different, the SSFR distribution of RQ AGN appears to be similar to both SFGs and, if to a lesser extent, to RL AGN, when infrared-based star formation rates are being used. The $\mathrm{SSFR_{IR}}$ distribution of RQ AGN is thus somewhat intermediate between that of SFGs and that of RL AGNs.

It should also be noted that both our SFGs and RQ AGN samples lie a little above the MS of SFGs. Bonzini et al. (2015) also found that their radio-selected SFGs and RQ AGN tend to have higher SFRs with respect to what is expected from the redshift evolution of the MS and attributed this bias towards high SFRs to their radio selection. The open red, open blue, and filled grey inset histogram in each panel shows the distribution for the RL AGN, RQ AGN, and SFGs in each redshift bin, respectively. The distribution of SFGs in each panel is scaled by a factor of five to ease the comparison to the RQ and RL AGN distributions. The three populations have by and large similar stellar mass distribution. We note that this is not what is typically expected, as RQ AGN (at least the ones found at bright > 1 mJy radio fluxes, e.g. see Kozieł-Wierzbowska et al. 2017) and SFGs are generally found in lower mass host galaxies than RL AGN. However, perhaps because of our joint selection based on radio detection and $\mathrm{SFR_{IR}}$ estimate, particularly in the higher redshift bins where most of our sample lies the range of SFRs and thus of stellar masses probed by our sample is limited and biased towards higher values, making it difficult to distinguish different populations.

Fig. 8 plots stellar mass versus radio luminosity for SFGs, RQ AGN, and RL AGN, where colours are scaled according to redshifts. Below a stellar mass of $\sim 10^{10}\,\mathrm{M}_\odot$, the overwhelming majority of our objects are SFGs, which span a large range in stellar mass, particularly at $z < 0.5$. RQ and RL AGN are mostly found at higher redshifts and thus at higher stellar masses, and the most powerful RL AGN are only found in the most massive objects at $z > 2$. The trend in stellar mass versus radio luminosity for both RQ and RL AGN is much less pronounced than for SFGs, and particularly so for RQ AGN.

4 AGN RADIO LUMINOSITY FUNCTION (RLF)

In this section we describe the AGN sample selection used for computing the RLF. We explain the method used in computing the AGN luminosity function and the reasoning behind adopting the analytic form of our local AGN luminosity function at 610 MHz to fit our data. We elaborate our motive for applying a further rmag cut of 25 to our sample for completeness correction. We present the AGN RLF in different redshift bins. We further describe how the evolution of AGN luminosity function out to $z \sim 1.5$ is constrained.

4.1 RLF sample selection

The number and percentage of AGN with spectroscopic and photometric redshifts without any redshift and $r_{\rm AB} < 25$ cuts is summarized in Table 7(a). We demonstrated in Ocran et al. (2020b) that the redshift distribution of the SFGs clearly shows that the sample is incomplete for $r_{\rm mag} > 25$ and $z > 1.5$. This incompleteness is driven by HSC/Subaru photometric redshifts, which start being incomplete at $z \sim 1.3$. It is recommended by Tanaka et al. (2018) that photometric redshifts should only be used at $z \lesssim 1.5$ and $i \lesssim 25$. Table 7(b) summarizes the number and percentage of AGN with spectroscopic and photometric redshifts. In order to compute the AGN RLF, we select only AGN with $r_{\rm AB} < 25$ and $0.002 < z < 1.5$. The total number of AGN satisfying these criteria is 486 sources of which 287 sources are RL AGN whilst the remaining 199 sources are RQ AGN (see Table 7b). The $r_{\rm AB}$ magnitude distribution versus redshift for the RL and RQ AGN sample is plotted in the left-hand panel of Fig. 9. The $r_{\rm AB} = 25$ limit is indicated by the dashed horizontal black line. The right-hand panel of Fig. 9 shows the 610 MHz luminosity distribution versus redshift for our sample (after applying the magnitude cut $r_{\rm AB} < 25$).

4.2 Derivation of AGN RLF

We computed the volume densities (for a given redshift range) as described in detail in Ocran et al. (2020b). We followed the $\frac{1}{V_{\rm max}}$ approach (Schmidt 1968) and applied several corrections, including correcting for the incompleteness of our radio catalogue as well as optical identification and redshift incompletenesses which result from our sources not being identified or not being detected over a wide enough range of optical/IR wavelengths to compute a reliable (photometric) redshift. We refer to subsection 4.1 in Ocran et al. (2020b) for a comprehensive description of the procedure. The rest-frame 610 MHz luminosities were computed using the observed-frame 610 MHz flux densities and assuming a radio spectral index of $\alpha = -0.8$ (Ibar et al. 2010).

4.3 Local AGN RLF

Following Dunlop & Peacock (1990), we assume for the RLF a double power-law function, given by equation (8):

$$\Phi_0(L) = \frac{\Phi_\star}{(L_\star/L)^\alpha + (L_\star/L)^\beta}, \tag{8}$$

Table 5. Two-sided K–S statistics comparing the SFG&RQ AGN, SFG&RL AGN, and RQ AGN&RL AGN distributions in $\mathrm{SFR_{IR}[M_\odot yr^{-1}]}/M_\star(\mathrm{M_\odot})$ within each redshift interval.

Redshift	SFG&RQ AGN $\mathrm{SFR_{IR}(M_\odot yr^{-1})}/M_\star(\mathrm{M_\odot})$		SFG&RL AGN $\mathrm{SFR_{IR}(M_\odot yr^{-1})}/M_\star(\mathrm{M_\odot})$		RQ&RL AGN $\mathrm{SFR_{IR}(M_\odot yr^{-1})}/M_\star(\mathrm{M_\odot})$	
	K–S statistic	*p*-value	K–S statistic	*p*-value	K–S statistic	*p*-value
$0.002 < z < 0.25$	0.26	1.10×10^{-1}	0.36	1.49×10^{-4}	0.19	6.02×10^{-1}
$0.25 < z < 0.5$	0.22	6.00×10^{-2}	0.39	2.13×10^{-9}	0.29	1.80×10^{-2}
$0.5 < z < 0.9$	0.25	1.69×10^{-3}	0.29	1.86×10^{-7}	0.17	1.51×10^{-1}
$0.9 < z < 1.5$	0.10	3.23×10^{-1}	0.18	1.32×10^{-2}	0.18	6.98×10^{-2}

Table 6. Two-sided K–S statistics comparing the SFG&RQ AGN, SFG&RL AGN, and RQ AGN&RL AGN distributions in $\mathrm{SFR_{radio}(M_\odot yr^{-1})}/M_\star(\mathrm{M_\odot})$ within each redshift interval.

Redshift	SFG&RQ AGN $\mathrm{SFR_{radio}[M_\odot yr^{-1}]}/M_\star(\mathrm{M_\odot})$		SFG&RL AGN $\mathrm{SFR_{radio}[M_\odot yr^{-1}]}/M_\star(\mathrm{M_\odot})$		RQ&RL AGN $\mathrm{SFR_{radio}[M_\odot yr^{-1}]}/M_\star(\mathrm{M_\odot})$	
	K–S statistic	*p*-value	K–S statistic	*p*-value	K–S statistic	*p*-value
$0.002 < z < 0.25$	0.29	4.07×10^{-2}	0.40	1.71×10^{-5}	0.23	3.47×10^{-1}
$0.25 < z < 0.5$	0.16	2.84×10^{-1}	0.49	1.14×10^{-14}	0.36	1.48×10^{-3}
$0.5 < z < 0.9$	0.25	1.59×10^{-3}	0.38	2.44×10^{-12}	0.23	2.18×10^{-2}
$0.9 < z < 1.5$	0.11	2.35×10^{-1}	0.37	9.40×10^{-10}	0.32	6.70×10^{-5}

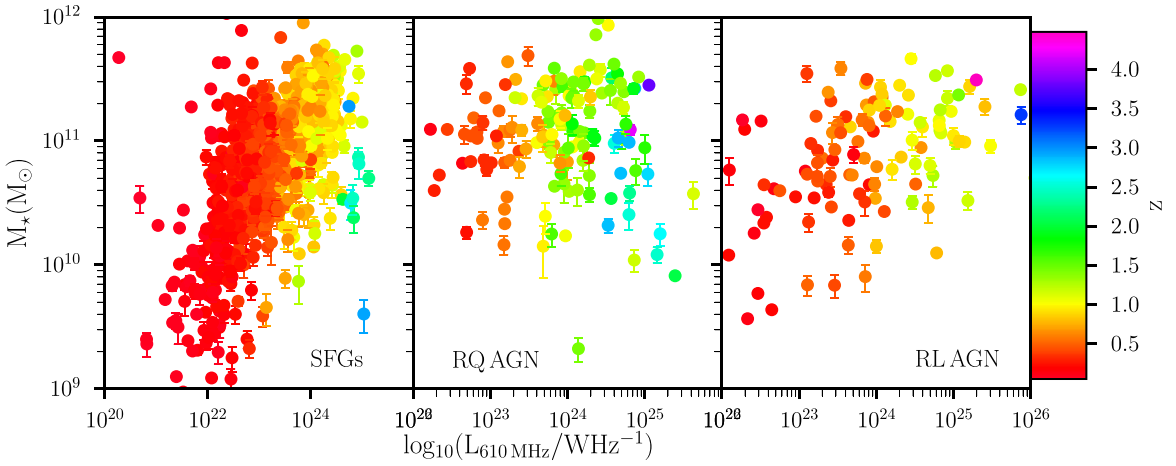

Figure 8. Stellar mass versus radio luminosity for SFGs (left-hand panel), RQ AGN (middle), and RL AGN (right-hand panel). Colour scale tracks redshift.

Table 7. Statistics of spectroscopic/photometric redshifts for the full AGN sample (i) and for the AGN sub-sample used to compute the RLF (ii) by selecting only AGN with $r_{\mathrm{AB}} < 25$ and $0.002 < z < 1.5$.

	RL AGN		RQ AGN	
	N	Per cent	*N*	Per cent
	All AGN (620 sources)			
z_{phot}	220	35.5	149	24.0
z_{spec}	118	19.0	133	21.5
	AGN used for RLF (486 sources)			
z_{phot}	177	36.4	107	22.0
z_{spec}	110	22.6	92	19.0

where $\Phi_\star$ is the normalization, $L_\star$ is the luminosity corresponding to the break in the LF whereas α and β are the bright- and faint-end slopes. We used this analytic form for the local AGN RLF and adopted here the fit from Mauch & Sadler (2007) where the parameters are $\Phi_\star = \frac{1}{0.4} 10^{-5.5}\,\mathrm{Mpc^3\,dex^{-1}}$ (scaled to the base of dlog L), $L_\star = 10^{24.59}\,\mathrm{W\,Hz^{-1}}$, $\alpha = -1.27$, and $\beta = -0.49$. We adopt the Mauch & Sadler (2007) for consistency with other studies in the literature. Mauch & Sadler (2007) constrain both the faint and bright end of the local AGN LF with a sample of 2661 detections in the 6dFGS-NVSS field with a median redshift of med(z) = 0.073 and a span of six decades in luminosities. Fig. 10 shows our local 610 MHz AGN luminosity function (open green squares). We truncate our sample at $z < 0.1$ to minimize the effects of evolution. The yellow plus symbols and blue stars represent the local LFs of Mauch & Sadler (2007) and Condon, Cotton & Broderick (2002). These LFs have are scaled from 1.4 GHz to 610 MHz assuming a spectral index of $\alpha = -0.8$. The solid red line represents the analytic fit to the local AGN LF of Mauch & Sadler (2007), converted to 610 MHz.

4.4 AGN RLF as a function of *z*

The AGN fitted radio luminosity functions at $\nu = 610$ MHz in different redshift bins are presented in Table 8 (for all AGN and for RQ and RL AGN separately) and in Fig. 11 (all AGN only;

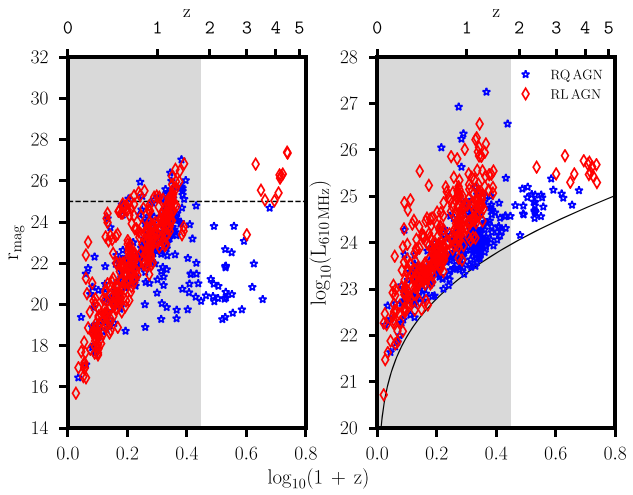

Figure 9. Left-hand panel: r_{AB} versus redshift for the RQ AGN (open blue stars) and RL AGN (open red diamonds) sample with redshift estimates. The dashed horizontal black line shows the magnitude limit of $r = 25$. Right-hand panel: 610 MHz luminosity versus redshift for the GMRT RQ and RL AGN sample with redshift. The black curve indicates the flux density limit plotted for $\alpha = -0.8$.

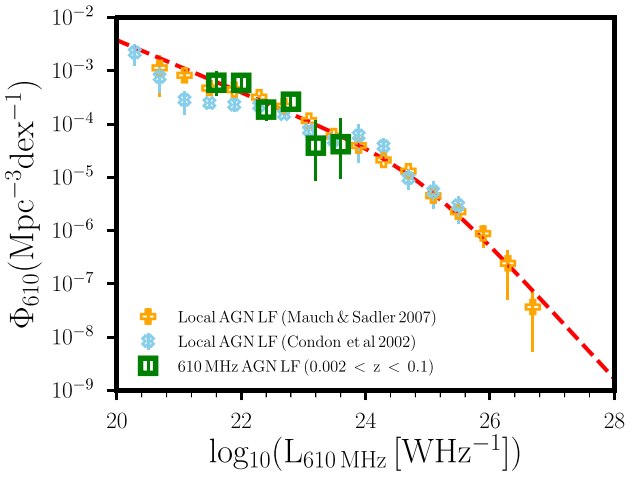

Figure 10. The local 610 MHz AGN luminosity function. The yellow plus symbols and blue stars represent the luminosity functions of Mauch & Sadler (2007) and Condon et al. (2002), respectively. The solid red line represents the analytic fit to the local 610 MHz AGN LF of Mauch & Sadler (2007). These have been scaled from 1.4 GHz to 610 MHz assuming a spectral index of $\alpha = -0.8$.

open green squares). Our data have small Poisson error bars due to the relatively large number of sources in each bin and as such the errors do not reflect all possible systematic effects. Scaled down luminosity functions from 1.4 GHz to 610 MHz (assuming $\alpha = -0.8$) by Smolčić et al. (2009), McAlpine, Jarvis & Bonfield (2013) and Smolčić et al. (2017) are shown as yellow pluses, light blue diamonds, and blue triangles, respectively, in each panel.

We also compare our AGN LFs with expectations from models and/or simulated radio catalogues, such as the AGN models by Mancuso et al. (2017) (see dot-dashed green line), the semi-empirical SKADS simulations by Wilman et al. (2008) (grey open pentagons), and the Tiered Radio Extragalactic Continuum Simulation (**T-RECS**) by Bonaldi et al. (2019) (black open diamonds) covering similar area and reaching similar depth in sensitivity and redshifts that we probe in this study. While we do not account for cosmic variance in our analysis (also in previous papers), according to the commonly adopted work by Driver & Robotham (2010) and Moster et al. (2011), the expected cosmic variance over our relatively large survey area and in our relatively large redshift bins is at the level of 5–10 per cent and thus will not affect our results disproportionately. In general, our RLFs agree well with other estimates from the literature, as well as with models, especially with the Bonaldi et al. (2019) one, which better follows the data at high luminosities. Bonaldi et al. (2019) described the cosmological evolution of the LF of RL AGN by adopting an updated version of the Massardi et al. (2010) model, slightly revised by Bonato et al. (2017). The relative fractions of the various classes in our sample used for computing the AGN LF is shown in Table 7(b) (see subsection 4.1). RL AGN constitute 287 sources with 177 sources having photometric redshifts and 110 sources having spectroscopic redshifts. RQ AGN constitute 199 sources with 107 sources having photometric redshifts and 92 sources having spectroscopic redshifts. Hence the agreement between the AGN population probed by the 610 MHz data in ELAIS N1 estimates with that of Bonaldi et al. (2019) can be attributed to the large RL AGN fraction in our sample with $L_{610\,MHz} \sim 10^{20} - 10^{27}\,\mathrm{W\,Hz^{-1}}$.

In the subsequent sections, we turn to study the evolution of AGN LFs in more detail. We first study the total AGN together. In the view of AGN having different classes with their widely different LFs and evolutions, we then examine the two classes (i.e. RL and RQ AGN) separately.

4.5 Evolution of AGN RLF

We model the evolution of the AGN RLF assuming pure luminosity evolution (PLE):

$$\Phi(L, z) = \Phi_0 \left[\frac{L}{(1+z)^{k_L(z)}}\right], \quad (9)$$

where $k_L = K_L + z\beta_L$; or pure density evolution (PDE):

$$\Phi(L, z) = (1+z)^{k_D(z)} \times \Phi_0(L), \quad (10)$$

where $k_D = K_D + z\beta_D$. We used the Markov chain Monte Carlo (MCMC) algorithm module EMCEE (Foreman-Mackey et al. 2013), implemented in the LMFIT Python package (Newville et al. 2014) to perform a multivariate fit to the data. The LMFIT Python package first does the fitting by performing a non-linear least-squares χ^2 minimization to obtain the best-fitting k_L and k_D parameters. The EMCEE is then implemented to calculate the probability distribution for the parameters. From this we get the medians of the probability distributions and a 1σ quantile, estimated as half the difference between the 15.8 and 84.2 percentiles. The solid red and dashed blue lines in each panel of Fig. 11 corresponds to the median values of the MCMC samples for the independent PLE and PDE fits in each redshift bin, respectively. The shaded regions correspond to the 68 per cent confidence region by combining PDE and PLE fitting to the samples. The dashed vertical pink and red lines in each panel of Fig. 11 shows the 5σ sensitivity limit (assuming a spectral index of $\alpha = -0.8$) at the low-redshift and high-redshift end of each redshift bin. Fig. 12 presents the best-fitting parameters obtained from fitting PLE (top panel) and PDE (bottom panel) models to the AGN luminosity functions. The open green squares in the top and bottom panels show the evolution parameters obtained from independently fitting the assumed analytic form of the luminosity function in four redshift bins assuming, respectively, pure luminosity and pure

Table 8. Luminosity functions of the total AGN, RQ AGN, and RL AGN samples obtained with the $1/V_{\rm max}$ method.

Redshift z	Luminosity $\log_{10}(L_{610\,\rm MHz}\,[\rm W\,Hz^{-1}])$	Number density $\Phi_{610}(\rm Mpc^{-3}dex^{-1})$ ALL AGN	Number N	Number density RQ AGN	Number	Number density RL AGN	Number
$0.002 < z < 0.25$	21.6	$5.99^{+4.07}_{-2.55} \times 10^{-4}$	4	$2.25^{+2.57}_{-1.32} \times 10^{-4}$	2	$3.74^{+4.26}_{-2.20} \times 10^{-4}$	2
	22.0	$6.09^{+2.81}_{-1.97} \times 10^{-4}$	7	$1.66^{+1.89}_{-0.90} \times 10^{-4}$	2	$4.43^{+2.57}_{-1.69} \times 10^{-4}$	5
	22.4	$2.75^{+0.95}_{-0.71} \times 10^{-4}$	11	$6.74^{+7.68}_{-3.96} \times 10^{-5}$	2	$2.08^{+0.81}_{-0.59} \times 10^{-4}$	9
	22.8	$3.59^{+0.90}_{-0.72} \times 10^{-4}$	18	$2.00^{+0.73}_{-0.54} \times 10^{-4}$	10	$1.59^{+0.67}_{-0.48} \times 10^{-4}$	9
	23.2	$1.19^{+0.61}_{-0.42} \times 10^{-4}$	6	$3.93^{+4.47}_{-2.31} \times 10^{-5}$	2	$7.98^{+5.42}_{-3.40} \times 10^{-5}$	4
	23.6	$4.27^{+4.87}_{-2.51} \times 10^{-5}$	2	–	–	$4.27^{+4.87}_{-2.51} \times 10^{-5}$	2
	24.0	$2.22^{+4.43}_{-1.73} \times 10^{-5}$	1	–	–	$2.22^{+4.43}_{-1.73} \times 10^{-5}$	1
	24.4	$4.47^{+5.09}_{-2.63} \times 10^{-5}$	2	–	–	$2.24^{+4.46}_{-1.74} \times 10^{-5}$	1
	24.8	$2.29^{+4.57}_{-1.78} \times 10^{-5}$	1	–			
$0.25 < z < 0.5$	22.8	$2.00^{+0.40}_{-0.34} \times 10^{-4}$	26	$9.49^{+2.79}_{-2.17} \times 10^{-5}$	14	$1.05^{+0.34}_{-0.26} \times 10^{-4}$	12
	23.2	$1.58^{+0.24}_{-0.21} \times 10^{-4}$	41	$5.64^{+1.66}_{-1.29} \times 10^{-5}$	14	$1.01^{+0.20}_{-0.17} \times 10^{-4}$	27
	23.6	$7.03^{+1.66}_{-1.35} \times 10^{-5}$	20	$1.40^{+0.95}_{-0.60} \times 10^{-6}$	4	$5.63^{+1.53}_{-1.22} \times 10^{-5}$	16
	24.0	$4.34^{+1.41}_{-1.07} \times 10^{-5}$	12	$3.47^{+6.92}_{-2.70} \times 10^{-6}$	1	$4.00^{+1.37}_{-1.03} \times 10^{-5}$	11
	24.4	$1.97^{+1.15}_{-0.75} \times 10^{-5}$	5	–	–	$1.97^{+1.15}_{-0.75} \times 10^{-5}$	5
	24.8	$8.02^{+9.14}_{-4.71} \times 10^{-6}$	2	–	–	$8.02^{+9.14}_{-4.71} \times 10^{-6}$	2
	25.2	$3.99^{+7.95}_{-3.10} \times 10^{-6}$	1	–	–	$3.99^{+7.95}_{-3.10} \times 10^{-6}$	1
	25.6	$4.14^{+8.26}_{-3.22} \times 10^{-6}$	1	–	–	$4.14^{+8.26}_{-3.22} \times 10^{-5}$	1
$0.5 < z < 0.9$	23.2	$9.66^{+2.52}_{-2.01} \times 10^{-5}$	17	$6.50^{+2.01}_{-1.54} \times 10^{-5}$	13	$3.16^{+2.15}_{-1.35} \times 10^{-5}$	4
	23.6	$7.43^{+1.00}_{-0.88} \times 10^{-5}$	52	$3.04^{+0.74}_{-0.60} \times 10^{-5}$	13	$4.39^{+0.77}_{-0.65} \times 10^{-5}$	33
	24.0	$4.59^{+0.63}_{-0.55} \times 10^{-5}$	50	$1.58^{+0.41}_{-0.33} \times 10^{-5}$	17	$3.01^{+0.53}_{-0.45} \times 10^{-5}$	33
	24.4	$2.11^{+0.46}_{-0.38} \times 10^{-5}$	23	$5.42^{+2.78}_{-1.89} \times 10^{-5}$	6	$1.57^{+0.41}_{-0.33} \times 10^{-5}$	17
	24.8	$1.16^{+0.38}_{-0.29} \times 10^{-5}$	12	–	–	$1.16^{+0.38}_{-0.29} \times 10^{-5}$	12
	25.2	$1.01^{+0.37}_{-0.27} \times 10^{-5}$	10	–	–	$1.01^{+0.37}_{-0.27} \times 10^{-5}$	10
	26.0	$3.14^{+2.64}_{-1.54} \times 10^{-6}$	3	–	–	$2.07^{+2.36}_{-1.22} \times 10^{-6}$	2
$0.9 < z < 1.5$	23.6	$5.10^{+1.50}_{-1.17} \times 10^{-5}$	14	$4.70^{+1.45}_{-1.12} \times 10^{-5}$	13	–	–
	24.0	$2.59^{+0.42}_{-0.36} \times 10^{-5}$	38	$2.39^{+0.40}_{-0.34} \times 10^{-5}$	35	–	–
	24.4	$1.51^{+0.24}_{-0.20} \times 10^{-5}$	40	$7.24^{+1.77}_{-1.42} \times 10^{-6}$	19	$7.87^{+1.83}_{-1.47} \times 10^{-6}$	21
	24.8	$1.14^{+0.20}_{-0.17} \times 10^{-5}$	32	$4.61^{+1.42}_{-1.09} \times 10^{-6}$	13	$6.76^{+1.65}_{-1.33} \times 10^{-6}$	19
	25.2	$4.44^{+1.44}_{-1.10} \times 10^{-6}$	12	$7.36^{+8.39}_{-4.33} \times 10^{-7}$	2	$3.70^{+1.35}_{-1.00} \times 10^{-6}$	10
	25.6	$1.98^{+1.15}_{-0.76} \times 10^{-6}$	5	$4.02^{+8.01}_{-3.12} \times 10^{-7}$	1	$1.58^{+1.07}_{-0.67} \times 10^{-5}$	4
	26.0	$2.42^{+1.24}_{-0.84} \times 10^{-6}$	6	–	–	$2.42^{+1.24}_{-0.84} \times 10^{-6}$	6
	26.4	$2.06^{+1.19}_{-0.79} \times 10^{-6}$	5	–	–	$1.23^{+1.03}_{-0.59} \times 10^{-6}$	3

density evolution. The vertical error bars in each panel represent the MAD of the MCMC samples. As shown in Fig. 12 and reported in Table 9 best fit PLE and PDE parameters show a fairly mild evolution when fitting the LF independently in each redshift bin. The solid red and blue lines in the two panels show the results obtained assuming linear PLE or PDE with redshift as in equations (9) and (10). In this case we derive $L_{610\,\rm MHz} \propto (1+z)^{(3.45\pm0.53)-(0.55\pm0.29)z}$ (i.e. $K_{\rm L} = 3.45 \pm 0.53$) and $\Phi \propto (1+z)^{(2.25\pm0.38)-(0.63\pm0.35)z}$ (i.e. $K_{\rm D} = 2.24 \pm 0.38$) for $0.002 < z < 1.5$.

5 DISCUSSION

5.1 Evolution of the total AGN population

Our 610 MHz RLF estimates seems to be in better agreement with the literature, but we caveat that RLF estimates we compare to are better constrained at higher frequency (1.4 GHz) and their extrapolation to much lower frequency heavily relies on the assumptions on the spectral index source distribution. We have scaled the 1.4 GHz flux densities to 610 MHz with our adopted fiducial spectral index of −0.8. Hence this broad agreement between the 610 MHz radio source population at very faint flux densities, limiting our sample to $z \sim 1.5$ and the literature cannot entirely be a one-to-one comparison.

Strazzullo et al. (2010) employed a method based on SED template fitting to separate their very faint radio sample ($5\sigma \sim 14\,\mu$Jy) into red, green, and blue populations, and found pure luminosity evolution of $K_{\rm L} \sim 2.7$ for the AGN-like red population. Padovani et al. (2011) measured pure luminosity evolution for their radio-quiet quasar sample and found that the low-luminosity radio-loud AGN population undergoes no evolution in the redshift range probed by the Smolčić et al. (2009) study, and suggesting that the evolution detected for low-luminosity AGN in the COSMOS study is driven by radio-quiet AGN included by their selection criteria.

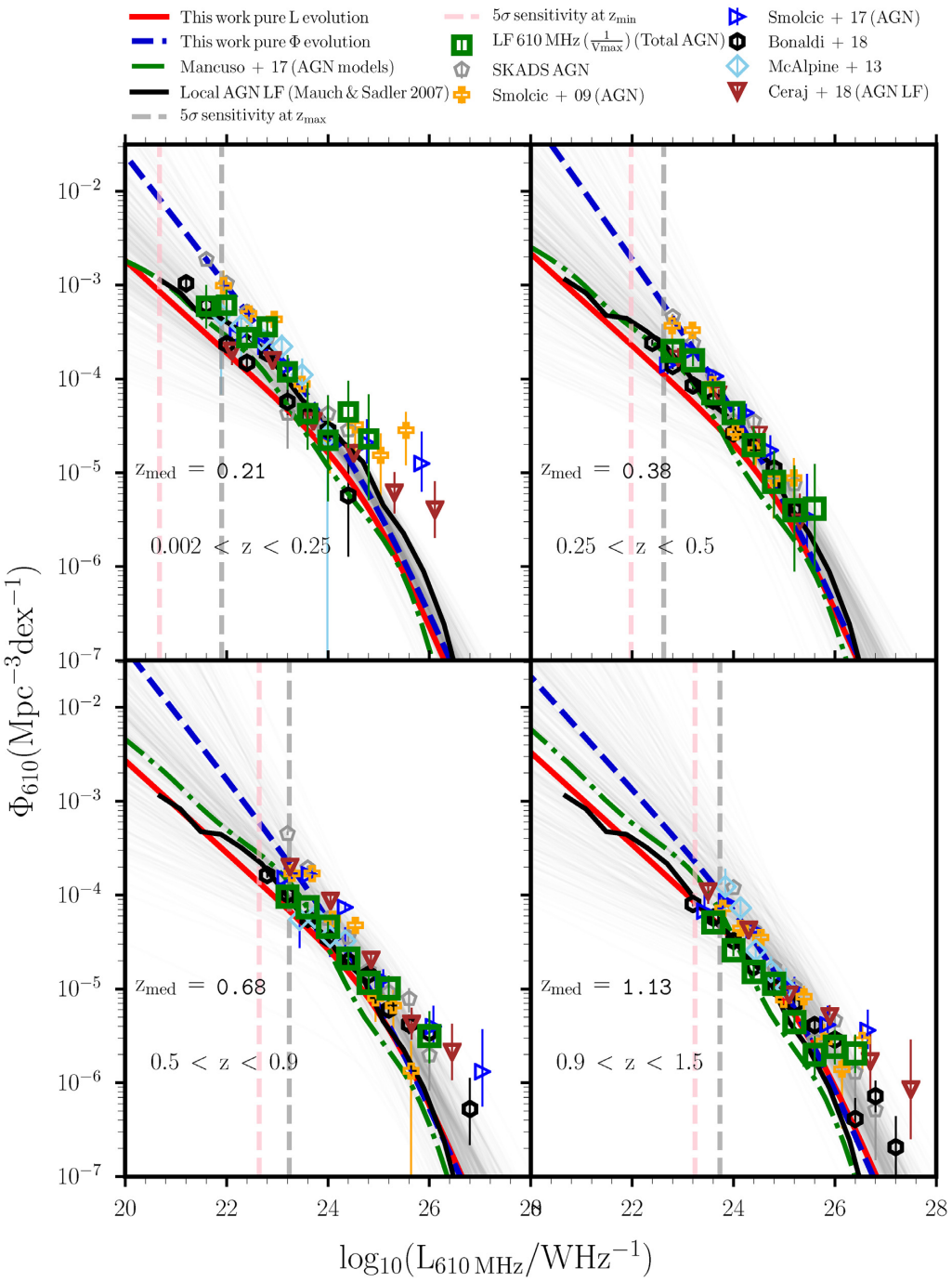

Figure 11. Radio luminosity functions of AGN at $\nu = 610$ MHz in different redshift bins (green open squares). The grey pentagons represent the total AGN LF from the semi-empirical simulation of the SKA (Wilman et al. 2008). The total AGN (i.e. RS AGN+RL AGN+RQ AGN) from Mancuso et al. (2017) models are represented by the dotted dashed green lines. Luminosity functions computed for AGN from the T-RECS (Bonaldi et al. 2019) simulations are shown as open black diamonds. The redshift range and the median redshift are shown in each panel. Error bars are determined using the prescription of Gehrels (1986). The local radio luminosity function of Mauch & Sadler (2007) is shown for reference as a solid black line in each panel. Scaled down luminosity functions from 1.4 GHz to 610 MHz by Smolčić (2009), Smolčić et al. (2017), and Ceraj et al. (2018) are shown as yellow pluses, right pointing blue triangles and downward pointing brown triangles, respectively, in each panel. The solid red and dashed blue lines in each panel correspond to the median values of the MCMC samples for the independent PLE and PDE fits in a given redshift bin, respectively.The dashed vertical pink and red lines in each panel shows the 5σ sensitivity limit (assuming a spectral index of $\alpha = -0.8$) at the low-redshift and high-redshift end of each redshift bin. The grey lines correspond to 1000 samples from the MCMC fits by a combination of PDE and PLE. See subsection 4.5.

Smolčić et al. (2017) constrained the evolution of this population via continuous models of pure density and pure luminosity evolutions on the 3 GHz COSMOS data, and found best-fitting parametrizations of $\Phi^\star \propto (1+z)^{(2.00\pm1.8)-(0.60\pm0.14)z}$ and $L^\star \propto (1+z)^{(2.88\pm0.82)-(0.84\pm0.34)z}$, respectively, with a turnover in number and luminosity densities of the population at $z \approx 1.5$. Ceraj et al. (2018) derived the 1.4 GHz AGN luminosity function of the full VLA-COSMOS 3 GHz Large Project sample with COSMOS2015

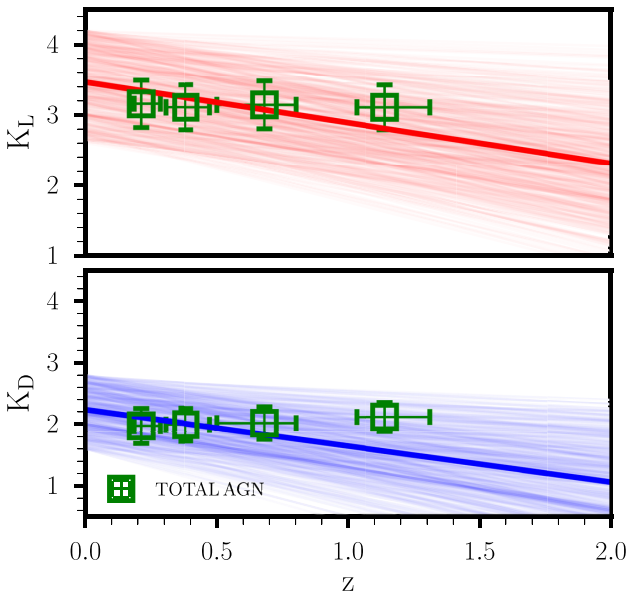

Figure 12. Parameters obtained by fitting PLE (top panel) and PDE (bottom panel) model to the AGN luminosity functions. The open green squares in both panels show the evolution parameters obtained from fitting the assumed analytic form of the luminosity function in four redshift bins assuming pure luminosity evolution and pure density evolution (see the text for details). The vertical error bars represent the MAD of the MCMC samples. The horizontal error bars denote the interquartile range (IQR) of redshift in each bin. The solid red (top panel) and blue (bottom) lines show the results from the continuous fit assuming that both the PLE and PDE parameters evolves linearly with redshift.

Table 9. Best-fitting evolution parameters obtained by fitting the local luminosity function to each redshift bin independently, assuming pure density K_D and pure luminosity K_L evolution.

Med(z)	K_D	K_L
$0.21^{+0.07}_{-0.03}$	1.94 ± 0.27	3.13 ± 0.33
$0.38^{+0.09}_{-0.08}$	1.98 ± 0.27	3.15 ± 0.33
$0.68^{+0.12}_{-0.18}$	1.99 ± 0.26	3.19 ± 0.34
$1.14^{+0.17}_{-0.11}$	2.09 ± 0.25	3.24 ± 0.32

counterparts out to $z \sim 6$ (shown as downward pointing brown triangles in Fig. 12), and found $\Phi^\star \propto (1+z)^{(1.24\pm0.08)-(0.25\pm0.03)z}$ and $L^\star \propto (1+z)^{(1.97\pm0.10)-(0.46\pm0.04)z}$, respectively. The COSMOS data at 3 GHz also probe very faint radio sources, but selecting objects at 3 GHz is biased towards more compact objects whereas selecting at 610 MHz reveals more of the diffuse radio emission missing from higher frequencies.

Even though we find evidence in support that some of these previous studies are broadly consistent with our radio derived PLE parameter, there are still studies from the literature that are not consistent with our work. Using the VLA-COSMOS 1.4 GHz survey Smolčić (2009) have derived luminosity functions for their rest-frame colour selected AGN out to $z = 1.3$, which is shown in Fig. 11 as open yellow pluses. Overall, the shape of the LF derived from their shallow 1.4 GHz survey follows the deep 610 MHz RLF study presented here in relatively similar redshift bins. However, they reported PLE and PDE evolution to be $L^\star \propto (1+z)^{0.8\pm0.1}$ and $\Phi^\star \propto (1+z)^{1.1\pm0.1}$, respectively. McAlpine et al. (2013) combined a 1 square degree VLA radio survey, complete to a depth of 100 μJy, with accurate 10 band photometric redshifts from the VIDEO and CFHTLS surveys. Their evolution is best fitted by an AGN PLE model $(1+z)^{1.18\pm0.21}$ out to $z \sim 2.5$. Prescott et al. (2016) detected mild but poorly constrained evolution from fits to their 325 MHz RLF for AGN out to $z = 0.5$, with evolution parameters of $K_D = 0.92 \pm 0.95$ for PDE and $K_L = 2.13 \pm 1.96$ for PLE.

Table 10 presents a tabulated summary of our results in the context of previous studies.

5.2 RL AGN evolution

The RL AGN (open red diamonds) luminosity function is presented in Fig. 13 at $\nu = 610$ MHz in different redshift bins. We compare our results to Mancuso et al. (2017) (see dotted dashed brown lines), who used the empirical description of the cosmological evolution for RL objects derived by Massardi et al. (2010). These have been extensively tested against a wealth of data on luminosity function and redshift distributions at least out to redshift $z \lesssim 3$ (see Massardi et al. 2010; Mancuso et al. 2017). Mancuso et al. (2017) model AGN in three components: radio silent (RS) AGN (we will return to the definition of RS AGN in subsection 5.3), RQ AGN, and RL AGN. Massardi et al. (2010) considered two flat-spectrum populations with different evolutionary properties, namely, flat-spectrum radio quasars (FSRQs) and BL Lacs, and a single steep-spectrum population (SSAGN). The comoving luminosity function at a given redshift was described by a double power law (we defer the reader to Massardi et al. 2010 for a full description of this procedure). We also compare our RL AGN LF to the LFs computed for RL AGN by Bonaldi et al. (2019) (from the T-RECS simulations, shown as open black hexagons). Bonaldi et al. (2019) described the cosmological evolution of the LF of RL AGN by adopting an updated version of the Massardi et al. (2010) model, slightly revised by Bonato et al. (2017), which includes the three source populations of Mancuso et al. (2017), with different evolutionary properties: steep-spectrum sources, flat-spectrum radio quasars, and BL Lacs. The best-fitting values of the parameters were re-computed adding to the fitted data sets the 4.8 GHz number counts for the flat-spectrum population by Tucci et al. (2011). This addition resulted in a significant improvement of the evolutionary model for flat-spectrum sources. Our RL AGN LFs are consistent with the improved results by Bonaldi et al. (2019), whereas they are higher than the model predictions by Mancuso et al. (2017). Ceraj et al. (2018) use the AGN-related 1.4 GHz emission to derive the 1.4 GHz AGN luminosity functions of moderate-to-high radiative luminosity active galactic nuclei (HLAGNs[2]) out to $z \sim 6$ (see downward pointing green triangles in Fig. 13) selected at 3 GHz within the VLA-COSMOS 3 GHz Large Project. They reported best-fitting parameters obtained with a continuous fit of the analytic form of $L^\star \propto (1+z)^{(3.97\pm0.15)-(0.92\pm0.06)z}$ in the case of pure luminosity evolution (i.e. $K_d = \beta_d = 0$).

The open red diamonds in Fig. 14 represent best-fitting k_L parameters obtained from fitting the PLE model to the RL AGN luminosity functions, independently in each redshift bin. From the independent

[2]HLAGN were identified by Ceraj et al. (2018) using a combination of X-ray (Civano et al. 2016) ($L_X > 10^{42}$ergs^{-1}) and MIR (Steinhardt et al. 2014) (colour–colour diagram; Donley et al. 2012) criteria and template fitting to the optical-to-millimetre spectral energy distributions (SED; Delvecchio et al. 2017)

Table 10. Comparison of the evolution parameters for radio AGN luminosity function determined from previous studies.

Reference	Field	Flux density limit	Wavelength	Redshift range	Sample size	PLE	PDE
Brown et al. (2001)	SGP&F855	5 mJy	1.4 GHz	$0.0 < z < 0.4$	230	3–5	–
Smolčić et al. (2009)	COSMOS	5 μJy	1.4 GHz	$0.1 < z < 1.3$	601	0.8 ± 0.1	1.1 ± 0.1
Padovani et al. (2011)[a]	CDFS	43 μJy	1.4 GHz	$0.1 < z < 5.8$	86	$3.5^{+0.4}_{-0.7}$	-1.8 ± 0.4
McAlpine et al. (2013)	VIDEO	100 μJy	1.4 GHz	$0 < z < 2.5$	951	1.18 ± 0.21	–
Padovani et al. (2015)[a]	E-CDFS	32.5 μJy	1.4GHz	$0.1 < z < 4.5$	136	-6.0 ± 1.4	-2.4 ± 0.3
Prescott et al. (2016)[b]	Three GAMA fields	∼5 mJy	325 MHz	$0.0 < z < 0.5$	428	2.13 ± 1.96	0.92 ± 0.95
Smolčić et al. (2017)[c]	COSMOS	∼ 2.3 μJy	3 GHz	$0.1 < z < 5$	1800	$(2.88 \pm 0.82) - (0.84 \pm 0.34)$z	$(2.00 \pm 1.8) - (0.60 \pm 0.14)$z
Ceraj et al. (2018)[c]	COSMOS	∼ 2.3 μJy	3 GHz	$0.1 < z < 6$	1604	$(3.97 \pm 0.15) - (0.92 \pm 0.06)$z	$(2.64 \pm 0.10) - (0.61 \pm 0.04)$z
This work (All AGN)[d]	ELAIS N1	∼7.1 μJy	610 MHz	$0.002 < z < 1.5$	486	$(3.45 \pm 0.53) - (0.55 \pm 0.29)$z	$(2.24 \pm 0.38) - (0.63 \pm 0.35)$z
This work (RQ AGN)[e]	–	–	–	–	199	$(2.81 \pm 0.43) - (0.57 \pm 0.30)$z	–
This work (RL AGN)[e]	–	–	–	–	287	$(3.58 \pm 0.54) - (0.56 \pm 0.29)$z	–

Notes. [a]flux density limit at the field centre.
Note. [b]minimum rms noise.
Note. [c]median rms for the 3 GHz VLA COSMOS.
Note. [d]minimum rms of the ∼1.86 deg^2 ELAIS N1 field.
Note. [e]the RL/RQ AGN cover similar redshift range, i.e. $0.002 < z < 1.5$.
SGP&F855 – South Galactic Pole (SGP) and UK Schmidt field 855 (F855).
COSMOS – Cosmological Evolution Survey.
CDFS – Chandra Deep Field South.
E-CDFS – Extended Chandra Deep Field South.
VIDEO – VISTA Deep Extragalactic Observations.

PLE parameters in the redshift $z \sim 0.002 - 0.25$, $z \sim 0.25 - 0.5$, $z \sim 0.5 - 0.9$, and $z \sim 0.9 - 1.5$ bins, we see a fairly mild evolution in radio luminosity (see also values in the third and fourth columns of Table 11).

We also derived a best-fitting $k_{\rm L}$ parameter obtained by continuous fitting of the PLE model to the redshift-dependent RL AGN luminosity functions. The light red lines show the results of 1000 MCMC realizations from the continuous fit assuming that the PLE parameter evolves linearly with redshift by using equation (9). The solid red line represents the median value of the MCMC samples. The vertical error bars are as described in Section 5.1. We derive $L_{610\,\rm MHz} \propto (1+z)^{(3.58\pm0.54)-(0.56\pm0.29)z}$ (i.e. $K_{\rm L} = 3.58 \pm 0.54$) for $0.002 < z < 1.5$, which is in agreement with Ceraj et al. (2018) results for the redshift space we probe. However, it is important to point out that Ceraj et al. (2018) constrained their cosmic evolution out to $z \sim 6$ whereas in our study of the faint low-frequency regime is limited out to $z \sim 1.5$.

5.3 RQ AGN evolution

In subsections 3.2 and 3.3, we have shown that RQ AGN are quite similar to SFGs in that they obey the relation between star formation rate and radio emission, even though the presence of outliers indicates that they can also host an active nucleus contributing to the radio emission. Indeed, the processes responsible for the emission of RQ AGN, as well as their dichotomy with the RL AGN population, are still vigorously debated. At the core of the problem is the understanding of the interaction between black hole accretion and star-formation in galaxies, which in turn constrains the relative emission levels (see Padovani et al. 2015; Mancuso et al. 2017; White et al. 2017 and references therein). We provide an estimate of the evolution of RQ AGN in the radio band at 610 MHz, by modelling it as a PLE $L(z) \propto (1+z)^{K_L + z\beta_L}$. The RQ AGN (blue stars) luminosity function is presented in Fig. 13 at $\nu = 610$ MHz in different redshift bins. The open blue stars in Fig. 14 presents best-fitting parameters obtained from independently fitting PLE model to the RQ AGN luminosity functions in each redshift bin. The RQ AGN exhibit a trend similar to that of RL AGN, with a fairly mild evolution in radio luminosity (see also $K_{\rm L}$ values in the first and second columns of Table 11). The best-fitting evolution parameters presented in Table 11 indicate a substantially slower evolution of this population, for the redshift binned data (i.e. $z \sim 0.002 - 0.25$, $0.25 - 0.5$, $0.5 - 0.9$, $0.9 - 1.5$) assuming a pure luminosity evolution. Fig. 14 also presents the best-fitting evolution parameters obtained by continuously evolving the local luminosity function assuming PLE. The light blue lines in this figure correspond to 1000 MCMC realizations whereas the solid blue line represents the median value of the MCMC samples assuming that the PLE parameter evolves linearly with redshift (as mentioned in previous sections). We derive $L_{610\,\rm MHz} \propto (1+z)^{(2.81\pm0.43)-(0.57\pm0.30)z}$ (i.e. $K_{\rm L} = 2.81 \pm 0.43$) for $0.002 < z < 1.5$. Padovani et al. (2011) estimated the evolution of RQ AGN in the radio band, modelling it as a PLE and obtaining $K_{\rm L} = 2.5^{+0.4}_{-0.5}$, in the range $0.2 \lesssim z \lesssim 3.9$. Following upon the estimate of the evolution of RQ AGN in the radio band derived in Padovani et al. (2011, 2015) reported a PLE fit to their RQ AGN LF of $K_{\rm L} = 3.0 \pm 0.2$ from the $V_{\rm e}/V_{\rm a}$[3] analysis and $K_{\rm L} = 2.5 \pm 0.2$ from their maximum-likelihood analysis, over a $0.2 - 3.66$ redshift range. Our results are broadly consistent with these previous findings from the literature.

We also compare our results to both the RQ AGN LF (see dot-dashed light blue lines) and also RQ+RS AGN (see solid orange lines) models derived by Mancuso et al. (2017). The RS and RQ AGN components are defined by Mancuso et al. (2017) as AGN clearly detectable in X-rays at luminosities $L_{\rm X} \gtrsim 10^{42}$ erg s^{-1}, but the origin of their radio emission is mainly ascribed to the star formation in the host galaxy in the former and to the central AGN in the latter. The star formation triggered radio emission in RS AGN is described using the model-independent approach by Mancuso et al. (2016a,b). The AGN-triggered RQ AGN were modelled by converting the bolometric power in X-rays via the Hopkins, Richards & Hernquist (2007) correction, and then deriving the AGN radio luminosity by using the relation between rest-frame X-ray and 1.4 GHz radio luminosity observed for samples of RQ AGN by Panessa et al. (2015) (see also Brinkmann et al. 2000). The available statistics does not allow us to clearly discriminate between the two models, but a contribution of SF-driven AGN at the second redshift bin, i.e. $0.25 < z < 0.5$, and low luminosities (log(L) < 22) is certainly present. At higher

[3]$V_{\rm e}/V_{\rm a}$ is the ratio between enclosed and available volume, when there is not a single flux density limit

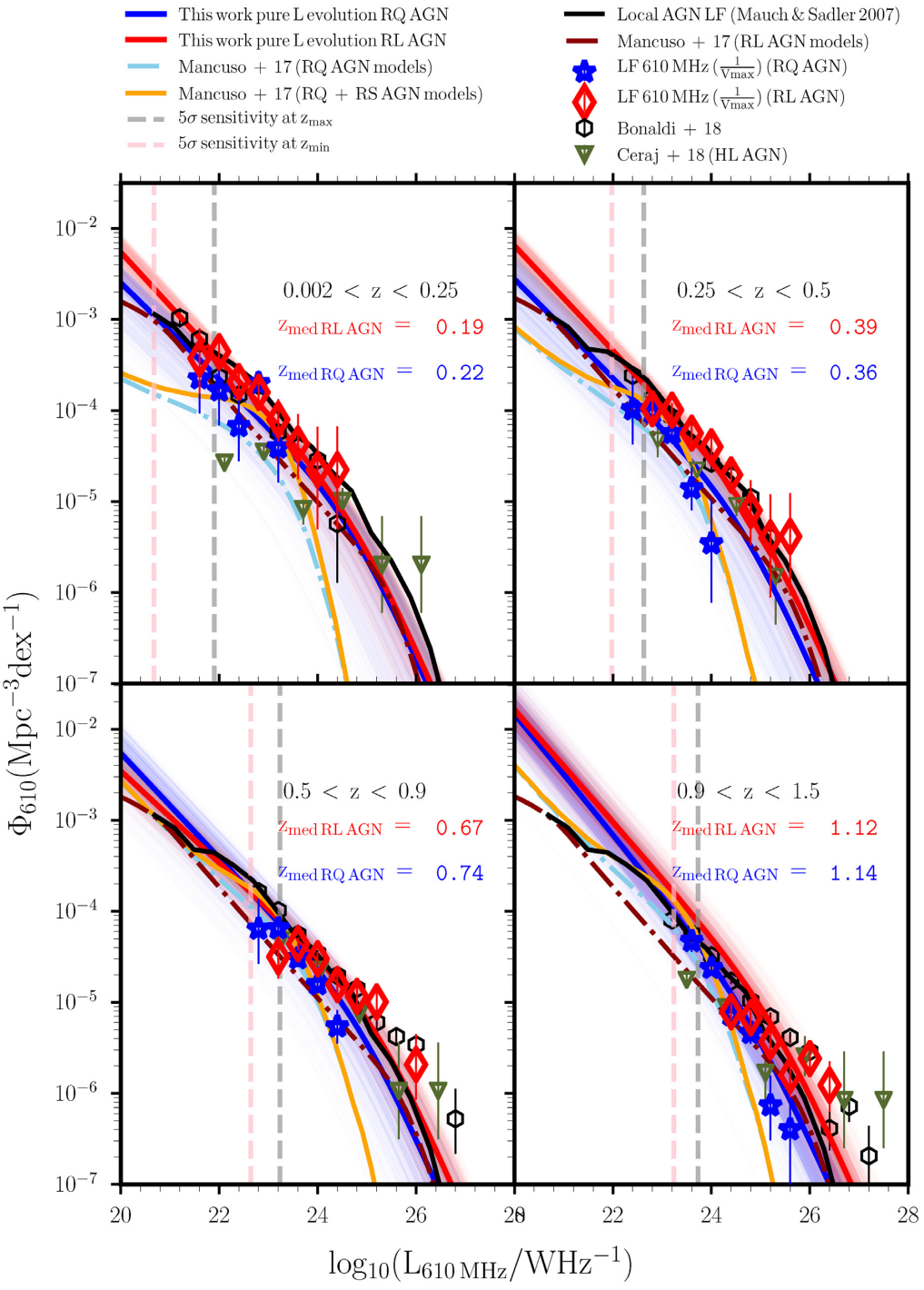

Figure 13. Radio luminosity functions of RL AGN (open red diamond) and RQ AGN (blue stars) at $\nu = 610$ MHz in different redshift bins. Luminosity functions computed for AGN from the T-RECS (Bonaldi et al. 2019) simulations are shown as open black hexagons. RL AGN and RQ AGN models from Mancuso et al. (2017) are represented, respectively, by the dot-dashed brown and light blue lines. The solid orange lines in each panel represents RS AGN+RQ AGN models from Mancuso et al. (2017). Error bars are determined using the prescription of Gehrels (1986). Scaled down HLAGN (see the text for details) luminosity functions from 1.4 GHz to 610 MHz by Ceraj et al. (2018) are shown as downward pointing green triangles in each panel. The local radio luminosity function of Mauch & Sadler (2007) is shown for reference as a solid black line in each panel. The solid red and blue lines in each panel correspond to the median values of the MCMC samples from the PLE fits to the RL and RQ AGN. The light red and blue lines in each panel corresponds 1000 MCMC realizations from the PLE fits. The dashed vertical pink and red lines in each panel shows the 5σ sensitivity limit (assuming a spectral index of $\alpha = -0.8$) at the low-redshift and high-redshift end of each redshift bin.

redshifts and higher luminosities this contribution seems to drop and become less significant.

Fig. 13 suggests that the division between RL and RQ AGN is indeed subjective. We see different populations hidden in the RQ AGN class, where the low luminosity end is dominated by SFGs. The high luminosity end is dominated by more AGN which could possibly be attributed to unresolved jets. Indeed larger samples can aid in the statistics such as the larger samples of radio-selected AGN

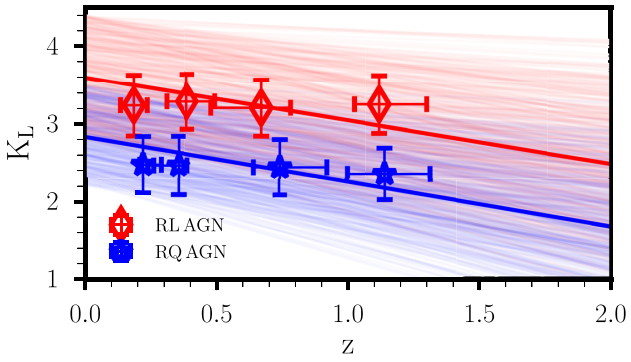

Figure 14. Parameters obtained by fitting PLE model to the RL and RQ AGN luminosity functions. The open red diamonds and blue stars show the evolution parameters obtained from fitting the assumed analytic form of the luminosity function in four redshift bins assuming pure luminosity evolution for both the RL and RQ AGN (see the text for details). The vertical error bars represent the MAD of the MCMC samples. The horizontal error bars denote the inter-quartile range (IQR) of redshift in each bin. The same colour line shows the results from the continuous fit assuming that the PLE parameter evolves linearly with redshift.

Table 11. Best-fitting evolution parameters obtained by the fitting local luminosity function to the redshift binned data assuming pure luminosity evolution (i.e. $K_{\rm L,RQAGN}$ $K_{\rm L,RLAGN}$).

$\rm Med(\mathit{z})_{RQAGN}$	$K_{\rm L,RQAGN}$	$\rm Med(\mathit{z})_{RLAGN}$	$K_{\rm L,RLAGN}$
$0.22^{+0.07}_{-0.01}$	2.43 ± 0.35	$0.19^{+0.05}_{-0.05}$	3.28 ± 0.38
$0.36^{+0.04}_{-0.09}$	2.45 ± 0.36	$0.39^{+0.08}_{-0.10}$	3.23 ± 0.37
$0.74^{+0.18}_{-0.10}$	2.42 ± 0.35	$0.67^{+0.19}_{-0.11}$	3.26 ± 0.36
$1.14^{+0.17}_{-0.14}$	2.47 ± 0.37	$1.12^{+0.10}_{-0.18}$	3.24 ± 0.36

we will have at the end of the still on-going MIGHTEE survey. This will greatly improve upon our work and will allow a better statistical analysis and a better estimate of the model parameters we present in this study. We acknowledge that separating the AGN populations into RL or RQ based on one criterion will not be robust and may not help in understanding the entire nature of these populations at these faint fluxes. We recommend that having understood the major difference between these two AGN classes through different multiwavelength diagnostics, future studies should concentrate on the physics and the long-standing question raised by Padovani (2017), which is: why only a minority of AGN have strong relativistic jets?

Although our results appear to be robust, there appears to be some interesting differences between SFGs, RL, and RQ AGN. Based on Section 3, we observe at the low redshift bin of the SFR $-$ $\rm M_\star$ plane, the RQ AGN population is made up by more massive galaxies than the SFGs in the same bin. The RL AGN population also has objects above the MS. On the contrary one might deduct the opposite given the median values of SFGs, RQ, and RL AGN in Section 3: that the RQ population is different while the RL and SFGs have similar $\rm SFR_{IR}(M_\odot yr^{-1})$ median values. The median values of $\log_{10}\rm M_\star(M_\odot)$ show a slight difference between the three populations. However, from the evolution of the RQ and RL AGN populations presented in this section we find that evolution of their LFs is different albeit these populations evolve fairly mildly with redshift. In Ocran et al. (2020b), we found a strong SFGs evolution trend with redshift. We acknowledge that sensitive radio continuum surveys that will be provided by the SKA will allow a better statistical analysis and understanding of the host properties of the RQ and RL AGN populations. To this end, larger samples of radio-selected, RQ, and RL AGN samples will put stronger constraints on the evolution of these sources.

6 SUMMARY AND CONCLUSIONS

We study a sample of 620 AGN selected over $\sim$1.86 deg^2 down to a minimum noise of $\sim$7.1 μJy beam^{-1} in the ELAIS N1 field at 610 MHz observed with the GMRT. The AGN sample was defined via a combination of diagnostics from the radio and X-ray luminosity, optical spectroscopy, mid-infrared colours, and 24 μm to radio flux ratios. Of the 620 AGN from our sample, 251 have spectroscopic redshifts whereas 369 have photometric redshifts. The AGN subsample is constructed based on a source having at least one multiwavelength AGN diagnostic and a redshift estimate. Sources meeting these criteria were further classified into RQ AGN (281 sources, or 45 per cent of the sample) and RL AGN (339 sources, or 55 per cent of the sample).

The principal results of our analysis are the following:

(i) We measure a median value of 2.10 ± 0.34 for the IRRC at 610 MHz for our RQ AGN population. This is comparable to that of our SFGs we measured in Ocran et al. (2020b) which was 2.32 ± 0.30. This suggests that the radio emission from RQ AGN host galaxies results primarily from star formation activity. The RL AGN, on the other hand, are systematically above the IRRC correlation for SFGs and RQ AGN, with a median value of 1.75 ± 0.40, indicating the presence of additional AGN-powered radio emission. The median values of the IRRC we measure for the RQ and RL AGN populations are somehow expected since the two populations are classified also on the basis of their radio excess or lack thereof.

(ii) We have shown that the radio and the IR are equivalently good tracers of the SFR for our SFGs and RQ AGN but not for the RL AGN. Both the radio and the IR seem as good tracers for RQ AGN and SFGs at low luminosities. However, at high $\rm SFR_{radio}$ all populations (i.e. SFGs, RQ, and RL AGN) deviate from the one-to-one relation. Even with this deviation, we find evidence in support of the argument that in RQ AGN the radio luminosity is tracing the SF activity in the host galaxy rather effectively but that in RL AGN the radio emission originates mainly from the extended radio structure, i.e. jets and lobes. Nevertheless, it is also possible for kpc-scale jets to contaminate the radio emission in RQ AGN, especially at high radio luminosity, where we see an increasing fraction of outliers with respect to the radio–FIR correlation. Our 610 MHz image shows a small number of bright classical radio galaxies with double-lobed and jet morphologies, most of which were classified as RL AGN (i.e. depending on whether they have a multiwavelength AGN diagnostic). The vast majority of the radio sources are faint objects that are unresolved at our $\sim$6 arcsec angular resolution. We compare the SFR derived from the IR luminosity and the radio power to show that the two are equivalently good tracers of star formation in non-active SFGs and also for the host galaxies of RQ AGN. The study of the correlation between galaxy SFR and stellar mass at different redshifts for our SFGs, RQ, and RL AGN show that the vast majority of our sources lie on the star formation main sequence when using infrared star formation rates, and that the $\rm SSFR_{IR}$ distribution of RQ AGN is somewhat intermediate between that of SFGs and that of RL AGNs.

(iii) We derived the AGN radio luminosity function of out to $z \sim 1.5$ using the $\frac{1}{V_{\rm max}}$ method by limiting the AGN sample to

sources satisfying a cut of $r_{\rm AB} < 25$ and $0.002 < z < 1.5$. We further constrained the evolution of this population with continuous models of pure density and pure luminosity evolution finding best-fitting parameters of $\Phi^{\star} \propto (1+z)^{(2.25\pm0.38)-(0.63\pm0.35)z}$ and $L_{610\,\rm MHz} \propto (1+z)^{(3.45\pm0.53)-(0.55\pm0.29)z}$. The AGN as a whole do not appear to evolve significantly in both PLE and PDE in the individual redshift bins we consider for this study. We assumed the local AGN RLF Mauch & Sadler (2007) of these two distinct populations and constrained the evolution of both the RQ and RL AGN population via continuous models of pure luminosity evolution. RL AGN exhibit a fairly mild evolution with redshift in radio luminosity as $\propto (1+z)^{(3.58\pm0.54)-(0.56\pm0.29)z}$, up to $z \sim 1.5$. RQ AGN also evolve fairly mildly with redshift in radio luminosity as $\propto (1+z)^{(2.81\pm0.43)-(0.57\pm0.30)z}$, up to $z \sim 1.5$. The fitted PLE evolution of our RQ AGN is comparable to that of our SFGs (i.e. $\propto (1+z)^{(2.95\pm0.19)-(0.50\pm0.15)z}$, see Ocran et al. 2020b).

(iv) Comparing our RLF for both the RQ AGN and RL AGN population to models by Mancuso et al. (2017) and Bonaldi et al. (2019), we find that our RQ AGN LFs in the different redshift bins for which the LFs are computed, are mostly consistent with the models predicted by Mancuso et al. (2017), while models by Bonaldi et al. (2019) seem to overpredict our RQ AGN LFs. On the other hand, the RL AGN LFs are higher than the Mancuso et al. (2017) estimates but agrees well with Bonaldi et al. (2019) models in different redshift bins. With respect to radio luminosity, the LFs of the RL AGN objects extends to higher radio luminosities whereas the RQ AGN dominates at lower radio luminosities. Thus, the host galaxies of RQ AGN exhibit very similar trends in radio luminosity to that of SFGs. The hosts of the RQ and RL AGN populations may differ in morphological type as Kozieł-Wierzbowska et al. (2017) showed that in their RL AGN sample the frequency of elliptical galaxies becomes larger with increasing radio loudness. Conversely, a rigid dichotomy that reflects the fundamental physical differences between RQ and RL AGN such as suggested by Padovani (2017) as classifying radio AGN as jetted and non-jetted sources is needed. While numerous studies have focused and agreed on many properties of RQ and RL AGN, the physical properties of such sources at these faint fluxes should indeed be the focus of current and future studies.

This work explores the nature of the faintest cosmic sources detected to date at low radio frequencies. This allowed a study of the evolution of the properties of the radio emission with cosmic time, including changes in the distribution of luminosities of the objects and in the rates of star formation. These data provide a first look at the faint radio sky at sensitivities that can now be achieved with LOFAR (van Haarlem et al. 2013) at 150 MHz, with the uGMRT (Gupta et al. 2017) at 325 and 610 MHz and with MEERKAT (Jonas & MeerKAT Team 2016) in the *UHF* and *L* bands, thus paving the way to the exploration of the deep and wide radio universe with the Square Kilometre Array (SKA; Braun et al. 2015, 2019). In future studies, we will use the ongoing MEERKAT International GHz Tiered Extragalactic Exploration (MIGHTEE) Survey (Jarvis et al. 2016) which has been planned with the goal of studying the formation and evolution of galaxies and AGN over cosmic time. MIGHTEE will greatly improve upon radio studies to date, and given appropriate ancillary multiwavelength data, have the potential of being able to assemble vast samples of AGN in the faint radio Universe. This will help us to expand this study to higher redshifts to constrain the cosmic evolution of the radio AGN population. Additionally, a parallel effort, known as superMIGHTEE, is also underway to obtain matched-resolution 610 MHz imaging of the MIGHTEE fields with the uGMRT. The upcoming deep surveys mentioned here will be complemented by very-wide-area surveys like the Evolutionary Map of the Universe (EMU) at 1.4 GHz and the VLA Sky Survey (VLASS) at 3 GHz, which will sample brighter and rarer populations.

ACKNOWLEDGEMENTS

EFO acknowledges financial support from the Inter-University Institute for Data Intensive Astronomy and from a University of Cape Town Astronomy Department Postgraduate Scholarship. CHIC acknowledges the support of the Department of Atomic Energy, Government of India, under the project 12-R&D-TFR-5.02-0700. We acknowledge support from the Italian Ministry of Foreign Affairs and International Cooperation (MAECI Grant Number ZA18GR02) and the South African Department of Science and Technology's National Research Foundation (DST-NRF Grant Number 113121) as part of the ISARP RADIOSKY2020 Joint Research Scheme. This work was carried out using the data processing pipelines developed at the Inter-University Institute for Data Intensive Astronomy (IDIA) and available at https://idia-pipelines.github.io. IDIA is a partnership of the University of Cape Town, the University of Pretoria, and the University of the Western Cape. We acknowledge the use of the ilifu cloud computing facility – http://www.ilifu.ac.za, a partnership between the University of Cape Town, the University of the Western Cape, the University of Stellenbosch, Sol Plaatje University, the Cape Peninsula University of Technology, and the South African Radio Astronomy Observatory. The ilifu facility is supported by contributions from the Inter-University Institute for Data Intensive Astronomy (IDIA – a partnership between the University of Cape Town, the University of Pretoria, and the University of the Western Cape), the Computational Biology division at UCT and the Data Intensive Research Initiative of South Africa (DIRISA). We also thank Anna Bonaldi for providing us her model predictions. We thank the staff of the GMRT that made these observations possible. GMRT is run by the National Centre for Radio Astrophysics of the Tata Institute of Fundamental Research. This work is based in part on observations made with the *Spitzer Space Telescope*, which is operated by the Jet Propulsion Laboratory, California Institute of Technology under a contract with NASA. Funding for the Sloan Digital Sky Survey IV has been provided by the Alfred P. Sloan Foundation, the U.S. Department of Energy Office of Science, and the Participating Institutions. SDSS-IV acknowledges support and resources from the Center for High-Performance Computing at the University of Utah. The SDSS web site is https://www.sdss.org.

DATA AVAILABILITY

The data underlying this article will be shared on reasonable request to the corresponding author.

REFERENCES

Appleton P. N. et al., 2004, ApJS, 154, 147
Banfield J. K., George S. J., Taylor A. R., Stil J. M., Kothes R., Scott D., 2011, ApJ, 733, 69
Becker R. H., White R. L., Helfand D. J., 1995, ApJ, 450, 559
Bell E. F., McIntosh D. H., Katz N., Weinberg M. D., 2003, ApJS, 149, 289
Bonaldi A., Bonato M., Galluzzi V., Harrison I., Massardi M., Kay S., De Zotti G., Brown M. L., 2019, MNRAS, 482, 2
Bonato M. et al., 2017, MNRAS, 469, 1912
Bonzini M., Padovani P., Mainieri V., Kellermann K. I., Miller N., Rosati P., Tozzi P., Vattakunnel S., 2013, MNRAS, 436, 3759
Bonzini M. et al., 2015, MNRAS, 453, 1079

Boquien M., Burgarella D., Roehlly Y., Buat V., Ciesla L., Corre D., Inoue A. K., Salas H., 2019, A&A, 622, A103
Bower R. G., Benson A. J., Malbon R., Helly J. C., Frenk C. S., Baugh C. M., Cole S., Lacey C. G., 2006, MNRAS, 370, 645
Braun R., Bourke T., Green J. A., Keane E., Wagg J., 2015, Proc. Sci., Advancing Astrophysics with the Square Kilometre Array (AASKA14), SISSA, Trieste, p. 174
Braun R., Bonaldi A., Bourke T., Keane E., Wagg J., 2019, preprint (arXiv: 1912.12699)
Brinchmann J., Charlot S., White S. D. M., Tremonti C., Kauffmann G., Heckman T., Brinkmann J., 2004, MNRAS, 351, 1151
Brinkmann W., Laurent-Muehleisen S. A., Voges W., Siebert J., Becker R. H., Brotherton M. S., White R. L., Gregg M. D., 2000, A&A, 356, 445
Brown M. J. I., Webster R. L., Boyle B. J., 2001, AJ, 121, 2381
Cannon R. et al., 2006, MNRAS, 372, 425
Ceraj L. et al., 2018, A&A, 620, A192
Chabrier G., 2003, Publ. Astron. Soc. Pac., 115, 763
Civano F. et al., 2016, ApJ, 819, 62
Condon J. J., 1992, ARA&A, 30, 575
Condon J. J., Cotton W. D., Greisen E. W., Yin Q. F., Perley R. A., Taylor G. B., Broderick J. J., 1998, AJ, 115, 1693
Condon J. J., Cotton W. D., Broderick J. J., 2002, AJ, 124, 675
Croton D. J. et al., 2006, MNRAS, 365, 11
Daddi E. et al., 2007, ApJ, 670, 156
de Jong T., Klein U., Wielebinski R., Wunderlich E., 1985, A&A, 147, L6
Delvecchio I. et al., 2017, A&A, 602, A3
Dickey J. M., Salpeter E. E., 1984, ApJ, 284, 461
Donley J. L. et al., 2012, ApJ, 748, 142
Driver S. P., Robotham A. S. G., 2010, MNRAS, 407, 2131
Dunlop J. S., Peacock J. A., 1990, MNRAS, 247, 19
Dunlop J. S., McLure R. J., Kukula M. J., Baum S. A., O'Dea C. P., Hughes D. H., 2003, MNRAS, 340, 1095
Elbaz D. et al., 2007, A&A, 468, 33
Foreman-Mackey D., Hogg D. W., Lang D., Goodman J., 2013, PASP, 125, 306
Gehrels N., 1986, ApJ, 303, 336
Giroletti M., Panessa F., 2009, ApJ, 706, L260
Griffin M. J. et al., 2010, A&A, 518, L3
Gupta Y. et al., 2017, Curr. Sci., 113, 707
Hopkins P. F., Richards G. T., Hernquist L., 2007, ApJ, 654, 731
Hurley P. D. et al., 2017, MNRAS, 464, 885
Ibar E., Ivison R. J., Best P. N., Coppin K., Pope A., Smail I., Dunlop J. S., 2010, MNRAS, 401, L53
Ishwara-Chandra C. H., Taylor A. R., Green D. A., Stil J. M., Vaccari M., Ocran E. F., 2020, MNRAS, 497, 5383
Jarvis M. et al., 2016, Proc. Sci., The MeerKAT International GHz Tiered Extragalactic Exploration (MIGHTEE) Survey, SISSA, Trieste, p. 006
Johnston R., Vaccari M., Jarvis M., Smith M., Giovannoli E., Häußler B., Prescott M., 2015, MNRAS, 453, 2540
Jonas J., MeerKAT Team, 2016, Proc. Sci., The MeerKAT Radio Telescope, SISSA, Trieste, p. 001
Kimball A. E., Kellermann K. I., Condon J. J., Ivezić Ž., Perley R. A., 2011, ApJ, 739, L29
Kozieł-Wierzbowska D., Vale Asari N., Stasińska G., Sikora M., Goettems E. I., Wójtowicz A., 2017, ApJ, 846, 42
Lacy M. et al., 2004, ApJS, 154, 166
Lee K.-S. et al., 2012, ApJ, 752, 66
Lopes M. E., Wang S., Mahoney M. W., 2019, J. Mach. Learn. Res., 20, 1
Małek K. et al., 2018, A&A, 620, A50
Mancuso C., Lapi A., Shi J., Gonzalez-Nuevo J., Aversa R., Danese L., 2016a, ApJ, 823, 128
Mancuso C., Lapi A., Shi J., Cai Z.-Y., Gonzalez-Nuevo J., Béthermin M., Danese L., 2016b, ApJ, 833, 152
Mancuso C. et al., 2017, ApJ, 842, 95
Massardi M., Bonaldi A., Negrello M., Ricciardi S., Raccanelli A., de Zotti G., 2010, MNRAS, 404, 532
Mauch T., Sadler E. M., 2007, MNRAS, 375, 931
McAlpine K., Jarvis M. J., Bonfield D. G., 2013, MNRAS, 436, 1084
Moster B. P., Somerville R. S., Newman J. A., Rix H.-W., 2011, ApJ, 731, 113
Neugebauer G., Miley G. K., Soifer B. T., Clegg P. E., 1986, ApJ, 308, 815
Newville M., Stensitzki T., Allen D. B., Ingargiola A., 2014, LMFIT: Non-Linear Least-Square Minimization and Curve-Fitting for Python, Available at: https: //zenodo.org/record/11813
Noeske K. G. et al., 2007, ApJ, 660, L43
Ocran E. F., Taylor A. R., Vaccari M., Green D. A., 2017, MNRAS, 468, 1156
Ocran E. F., Taylor A. R., Vaccari M., Ishwara-Chandra C. H., Prandoni I., 2020a, MNRAS, 491, 1127
Ocran E. F., Taylor A. R., Vaccari M., Ishwara-Chandra C. H., Prandoni I., Prescott M., Mancuso C., 2020b, MNRAS, 491, 5911
Padovani P., 1993, MNRAS, 263, 461
Padovani P., 2016, A&AR, 24, 13
Padovani P., 2017, Nat. Astron., 1, 0194
Padovani P., Ghisellini G., Fabian A. C., Celotti A., 1993, MNRAS, 260, L21
Padovani P., Mainieri V., Tozzi P., Kellermann K. I., Fomalont E. B., Miller N., Rosati P., Shaver P., 2009, ApJ, 694, 235
Padovani P., Miller N., Kellermann K. I., Mainieri V., Rosati P., Tozzi P., 2011, ApJ, 740, 20
Padovani P., Bonzini M., Kellermann K. I., Miller N., Mainieri V., Tozzi P., 2015, MNRAS, 452, 1263
Panessa F. et al., 2015, MNRAS, 447, 1289
Pilbratt G. L. et al., 2010, A&A, 518, L1
Polletta M. et al., 2007, ApJ, 663, 81
Prescott M. et al., 2016, MNRAS, 457, 730
Rawlings S., Saunders R., 1991, Nature, 349, 138
Renzini A., 2009, MNRAS, 398, L58
Richards G. T. et al., 2006, ApJS, 166, 470
Rodighiero G. et al., 2011, ApJ, 739, L40
Rousseeuw P. J., Croux C., 1993, J. Am. Stat. Assoc., 88, 1273
Rowan-Robinson M., Gonzalez-Solares E., Vaccari M., Marchetti L., 2013, MNRAS, 428, 1958
Sadler E. M. et al., 2007, MNRAS, 381, 211
Sajina A., Lacy M., Scott D., 2005, ApJ, 621, 256
Salim S. et al., 2007, ApJS, 173, 267
Sargent M. T. et al., 2010, ApJ, 714, L190
Schmidt M., 1968, ApJ, 151, 393
Shirley R. et al., 2019, MNRAS, 490, 634
Simpson J. M. et al., 2012, MNRAS, 426, 3201
Smolčić V., 2009, ApJ, 699, L43
Smolčić V. et al., 2009, ApJ, 696, 24
Smolčić V. et al., 2017, A&A, 602, A6
Steidel C. C., Sargent W. L. W., 1991, ApJ, 382, 433
Steinhardt C. L. et al., 2014, ApJ, 791, L25
Strazzullo V., Pannella M., Owen F. N., Bender R., Morrison G. E., Wang W.-H., Shupe D. L., 2010, ApJ, 714, 1305
Tanaka M. et al., 2018, PASJ, 70, S9
Taylor A. R. et al., 2007, ApJ, 666, 201
Tucci M., Toffolatti L., de Zotti G., Martínez-González E., 2011, A&A, 533, A57
Vaccari M., 2016, Proc. Sci., The Many Facets of Extragalactic Radio Surveys: Towards New Scientific Challenges (EXTRA-RADSUR2015), SISSA, Trieste, p. 27
van Haarlem M. P. et al., 2013, A&A, 556, A2
White S. V., Jarvis M. J., Häußler B., Maddox N., 2015, MNRAS, 448, 2665
White S. V., Jarvis M. J., Kalfountzou E., Hardcastle M. J., Verma A., Cao Orjales J. M., Stevens J., 2017, MNRAS, 468, 217
Wilman R. J. et al., 2008, MNRAS, 388, 1335
Wilson A. S., Colbert E. J. M., 1995, ApJ, 438, 62
Yuan Z., Wang J., Zhou M., Mao J., 2016, ApJ, 820, 65
Yun M. S., Reddy N. A., Condon J. J., 2001, ApJ, 554, 803

This paper has been typeset from a TEX/LATEX file prepared by the author.